European summer weather linked to North Atlantic freshwater anomalies in preceding years

Marilena Oltmanns[1], N. Penny Holliday[1], James Screen[2], Ben I. Moat[1], Simon A. Josey[1], D. Gwyn Evans[1], and Sheldon Bacon[1]

[1]National Oceanography Centre, Southampton, UK
[2]University of Exeter, Exeter, UK

Correspondence: Marilena Oltmanns (marilena.oltmanns@noc.ac.uk)

Abstract. Amplified Arctic ice loss in recent decades has been linked to increased occurrence of extreme mid-latitude weather. The underlying mechanisms remain elusive, however. One potential link occurs through the ocean as the loss of sea ice and glacial ice leads to increased freshwater fluxes into the North Atlantic. Thus, in this study, we examine the role of North Atlantic freshwater anomalies in medium-term climate trajectories and specifically assess their links to European summer

5   weather. Combining a comprehensive set of observational products, we show that stronger freshwater anomalies are associated with sharper sea surface temperature gradients over the North Atlantic in winter, destabilising the overlying atmosphere and inducing a northward shift in the North Atlantic Current. In turn, the jet stream over the North Atlantic is deflected northward in the following summers, leading to warmer and drier weather over Europe. Our results suggest that growing freshwater fluxes into the North Atlantic could initiate a chain of ocean-atmosphere feedbacks that increases the risk of heat waves and droughts

10   over Europe, and that could yield enhanced predictability of European summer weather, months to years in advance.

1   Introduction

Arctic near-surface temperature is currently warming twice as fast as the global average (Cohen et al., 2019), which manifests itself in an average sea ice volume loss of $3.0 \pm 0.2 \cdot 1000$ km^3 decade^{-1}, based on the period 1979 to 2018 (Kumar et al., 2020). Similarly large losses are observed for land ice, particularly from the Greenland ice sheet, amounting to $3.0 \pm 0.3 \cdot$

15   1000 km^3 decade^{-1}, based on the period 2003 to 2012 (Khan et al., 2015). Earlier studies noticed statistical links between an amplified sea ice loss at high latitudes and an increased occurrence of weather extremes at mid-latitudes (Francis and Vavrus, 2012; Tang et al., 2014; Screen and Simmonds, 2013; Cohen et al., 2014). However, the robustness of these links has been questioned and the underlying mechanisms are poorly understood (Barnes, 2013; Overland et al., 2015; Blackport and Screen, 2020).

20   One potential connection occurs through the ocean. Specifically, the loss of sea ice and glacial ice in the Arctic and sub-Arctic regions constitutes a source of freshwater for the North Atlantic (Bamber et al., 2018; Carmack et al., 2016). Large North Atlantic freshwater anomalies, moreover, were found to give rise to cold surface anomalies and the development of storms in the subpolar region in winter (Oltmanns et al., 2020). In turn, cold anomalies in the subpolar region in winter were found to

precede heat waves over Europe in the subsequent summer (Duchez et al., 2016; Mecking et al., 2019). The heat waves were
attributed to a stationary jet stream over the North Atlantic (Duchez et al., 2016) and were successfully reproduced in model
simulations initialised with the cold anomaly (Mecking et al., 2019). Thus, by triggering cold anomalies in winter, increased
surface freshening could initiate a deterministic chain of events that first leads to cold anomalies and storms in winter and then
heat waves in the subsequent summer.

While earlier studies support individual connections between the North Atlantic sea surface temperature (SST) and the jet
stream (Woollings et al., 2010), or between shifts in the jet stream and European heat waves (Dong et al., 2013; Gervais et al.,
2020), the role of freshwater in initiating this causal chain is unclear. Yet, given that the Arctic and sub-Arctic regions are
expected to continue to warm and release freshwater from melting sea ice and glacial ice into the North Atlantic, it is critical
to understand how the resulting feedbacks will affect weather in Europe.

The gap in our knowledge around the potential influences of North Atlantic freshwater anomalies on European summer
weather arises from the difficulty to observe and simulate salinity. Freshwater is advected into the subpolar region through
mesoscale eddies requiring a high grid spacing of $\sim$1/12° (Marzocchi et al., 2015; Böning et al., 2016; Müller et al., 2019).
Most current coupled global climate models have a coarser grid spacing, giving rise to salinity biases (Mecking et al., 2017;
Menary et al., 2015; Wu et al., 2018). Moreover, in-situ observations of sea surface salinity mostly stem from Argo floats and
cannot capture the high spatial variability at high temporal resolution. Lastly, satellite observations of sea surface salinity are
associated with large uncertainties and only available since 2009 (Bao et al., 2019; Xie et al., 2019).

Given the limitations associated with the currently available model and observational products of sea surface salinity, we
use a new approach to estimate freshwater variations, taking advantage of a dynamical constraint of the sea surface salinity
on the SST. In the subpolar region in winter, surface water is cooled by the atmosphere, becomes denser, and sinks. Enhanced
surface freshening reduces the surface density and thus requires additional cooling before the surface water is dense enough to
be mixed down. When salinity changes are the dominant driver of stratification changes, this constraint of freshwater on the
SST can be used to infer its variability using a mass balance analysis (Oltmanns et al., 2020).

In the following, we describe the involved data products (Section 2) and explain the approach to estimate freshwater variabil-
ity from a surface mass balance (Section 3). We then use the approach to identify freshwater anomalies, examine the associated
ocean-atmosphere evolution, and assess their links with European summer weather (Section 4). We conclude by discussing the
dynamical contribution of freshwater anomalies to the identified chain of events and their implications (Section 5).

2 Data

First, we describe the data products involved in this study. To examine the ocean-atmosphere feedbacks associated with fresh-
water anomalies, we focussed on the period since 1979, motivated by the increased data quality associated with the onset of
satellite observations in 1979. For assessing longer-term variations in North Atlantic freshwater variability, we also considered
the period since 1950.

2.1 Observations

The analysis of ocean variability includes a merged SST product consisting of Hadley Centre HadISST1 data (Rayner et al., 2003; Hurrell et al., 2008) and optimal-interpolated, remote sensing-based SST data from NOAA (Reynolds et al., 2002). The merged Hadley – NOAA data product has a monthly temporal resolution, a $1°$ x $1°$ spatial resolution and is available from https://gdex.ucar.edu/dataset/158_asphilli.html.

We further employed absolute dynamic topography data since 1993, derived from altimetry (Le Traon et al., 1998). Absolute dynamic topography represents the sea level anomaly with respect to the geoid and thus, the stream function of the geostrophic surface flow. It is used to assess changes in surface currents. The monthly, gridded, absolute dynamic topography dataset has a spatial resolution of $0.25°$ x $0.25°$ and is distributed by the Copernicus Marine Environment Monitoring Service (https://marine.copernicus.eu/).

In addition, we included in-situ hydrographic observations from a mixed-layer database derived from Argo float profiles (Holte et al., 2017), and raw Argo profiles. The data is used to compare freshwater anomalies, estimated from the mass balance analysis, with in-situ observations and to assess the vertical extent of air-sea coupling processes in summer. Argo data is available at http://www.argodatamgt.org.

The ocean data is complemented by monthly output from the ERA5 atmospheric reanalysis model from the European Centre for Medium-Range Weather Forecasts since 1979 (Hersbach et al., 2018). In addition to the standard variables from ERA5, we estimated the maximum Eady growth rate. The maximum Eady growth rate is used to assess the baroclinic instability in the atmosphere over increased meridional SST gradients. Following earlier studies (Lindzen and Farrell, 1980; Dierer et al., 2005), we estimated the maximum Eady growth rate in the 1000 hPa to 750 hPa layer with $\sigma_E \approx 0.31 \frac{f}{N} \mid \frac{u_{750} - u_{1000}}{z_{750} - z_{1000}} \mid$, where f is the Coriolis frequency, u is the zonal wind, z the height, N the Brunt-Väisälä frequency and the subscripts refer to the associated pressure levels.

A key parameter, used to derive freshwater indices, is the mean North Atlantic Oscillation (NAO) in summer, obtained from the National Oceanic and Atmospheric Administration (NOAA) Climate Prediction Center. The NAO index was calculated using Rotated Principal Component Analysis, applied to the monthly standardised 500 hPa geopotential height anomalies between $20°N$ and $90°N$ (Barnston and Livezey, 1987) and identified as the dominant mode of variability in the northern hemisphere. A detailed derivation can be found at https://www.cpc.ncep.noaa.gov/products/precip/CWlink/pna/nao.shtml.

2.2 Model simulations

While the study is based on observations, we included model simulations to address specific processes. Thus, we used the Greenland climate model MAR to assess potential causes of freshwater anomalies. We used version 3.12, run at a resolution of 20 km forced by the ERA5 reanalysis (Fettweis et al., 2017) and distributed by the Laboratory of Climatology at the University of Liège. For the purpose of this study, we considered the runoff over the full ice sheet from 1950 through to the end of 2022 at monthly resolution. The dataset is available at ftp://ftp.climato.be/fettweis/MARv3.12.

To investigate the role of the SST in driving the atmospheric circulation, we employed SST-forced simulations from ECHAM5 (Roeckner et al., 2003) and CAM5 (Neale et al., 2012), obtained from the Facility of Climate Assessments repository (Murray et al., 2020). The simulations were performed with the prescribed, observed SST and sea ice cover and time varying greenhouse gases and ozone. Further details on the experimental setup can be obtained from https://psl.noaa.gov/repository/entry/show?entryid=85181601-0435-40be-8461-e282ac884144. ECHAM5 was run with a horizontal grid spacing of 0.75° x 0.75°, 31 vertical levels and 50 ensemble members, and CAM5 was run with a horizontal grid spacing of 1° x 1°, 30 vertical levels and 40 ensemble members. We excluded other models from the repository that do not cover the period 1979–2018 or that do not include all investigated parameters.

2.3 Removing greenhouse gas effects

The recent period was characterised by a significant trend of increasing greenhouse gas concentrations, implying that the warming trend resulting from increased greenhouse gases could superimpose on a potential warming trend due to freshwater anomalies and distort their effect on European air temperatures. To reduce the influence of increasing greenhouse gas concentrations on European air temperatures, we subtracted regionally averaged trends from the air temperature, both in ERA5 and the model simulations. By using regional averages, we assumed that the trend of the direct, greenhouse gas-induced warming over Europe is distributed relatively uniformly.

We tested different regions and found that the results are not sensitive to the area that is used for the averaging, as long as it is sufficiently large. Here, we averaged over the main area of investigation from 25 °N to 65 °N and from 60 °W to 60 °E, resulting in an average trend of $\sim$0.03 °C year^{-1} in the 2-m air temperature from ERA5. Extending the region in any direction does not appreciably change this trend, nor the subsequent results, consistent with the assumption that the direct warming trend that is solely due to increasing greenhouse gases is distributed relatively uniformly.

Since the freshening of the subpolar North Atlantic exhibited a trend over the recent period (Tesdal et al., 2018), trends are part of the signal we are interested in. In contrast to greenhouse gas induced warming, however, we do not expect the freshwater trend to cause any net imbalance in the net surface energy budget. Instead, considering the delineated links between fresh and cold anomalies, the jet stream, and European summer weather, we expect freshwater anomalies in the North Atlantic to be linked to baroclinic instabilities in the atmosphere, which equally produce warming regions and cooling regions. Thus, by subtracting regionally-averaged signals, we filter out the uniform warming effect of increasing greenhouse gases from those associated with baroclinic wave activity.

Indeed, when we remove the trend in the air temperature prior to the analyses, we obtain a signal that is dynamically consistent across all investigated variables. If, on the other hand, we do not remove the trend in the air temperature, we still obtain the same patterns throughout the results but there would be a large-scale, uniform warming signal superimposed over the full domain.

We did not apply any other averaging, smoothing, filtering, or further preprocessing steps to the datasets.

3   Estimation of freshwater anomalies

The objective of this study is to investigate feedbacks initiated by freshwater anomalies. However, high-quality global salinity measurements have only been routinely available since 2002, and mostly in the open ocean from Argo floats. Moreover, satellite observations of the sea surface salinity are of relatively low accuracy and only available since 2009 (Bao et al., 2019; Xie et al., 2019). Considering the limitations associated with currently available salinity products, we use a surface mass balance analysis to estimate the variability of freshwater.

3.1   Mass balance

We start with a surface mass balance for the mixed layer in the subpolar region in winter (Fig. 1):

$$\int_{-h(t)}^{0} \frac{\partial \rho}{\partial t}\, dz = -\frac{B}{g} + A + M, \tag{1}$$

where ρ is the mixed layer density, h is the mixed layer depth, A corresponds to horizontal mass transports, g is the gravitational acceleration, B is the buoyancy flux through the surface, and M is the mass flux entrained through the base of the mixed layer (Gill, 2016). After integrating Eq. (1) over the mixed layer from summer to winter, we obtain:

$$\rho h = h_0 \rho_0 + \left(-\frac{B}{g} + A + M \right) \cdot dt, \tag{2}$$

where h_0 and ρ_0 represent a mixed layer depth and density before the winter, for instance in September, h and ρ refer to the depth and density in winter (January to March), and dt is the corresponding integration interval from summer to winter.
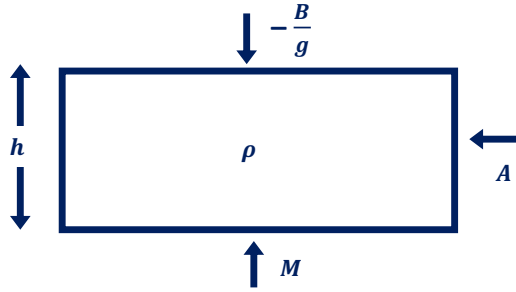
Figure 1. Mass budget for a mixed layer of depth h in the subpolar region, taking into consideration horizontal advection A, the density flux from beneath the mixed layer M, and the density contribution from the surface buoyancy flux $\frac{B}{g}$.

While the climatological mean mixed layer density increases during the winter, the mixed layer deepens. Thus, before the winter, the mixed layer is several tens of metres deep while during the winter, it reaches several hundred metres. Since the density anomaly in the initial shallow mixed layer becomes distributed over a much larger depth range, the first term on the righthand side is negligible compared to the other terms. Any density anomalies beneath the initial, shallow mixed layer are included in M.

We further separate each term into a mean and an anomaly n, with n referring to the n'th winter of an arbitrary subset of N winters and the mean representing the mean over these winters. Assuming that the mean state is in balance, we subtract the mean values from the resulting equation:

$$\rho_n h_{mean} + \rho_{mean} h_n + \rho_n h_n = \left(-\frac{B_n}{g} + A_n + M_n \right) \cdot dt. \tag{3}$$

Next, we linearise the equation of state around a reference state, which we choose to be the mean over the N selected winters: $\rho_n \approx \rho_{mean} \left(-\alpha \cdot T_n + \beta \cdot S_n \right)$, where T is the temperature, S is the salinity, α and β are the thermal and haline expansion coefficients. After plugging the linearised equation of state into the first term of Eq. (3), we obtain:

$$\rho_{mean} \left(-\alpha \cdot T_n + \beta \cdot S_n \right) \cdot h_{mean} + (\rho_{mean} + \rho_n) \cdot h_n \approx \left(-\frac{B_n}{g} + A_n + M_n \right) \cdot dt \tag{4}$$

The objective of this analysis is to find conditions (referred to as 'c'), in which the density anomalies associated with temperature anomalies are much larger than the effect of potential, active drivers of density anomalies on the righthand side of Eq. (4): $\rho_{mean} \cdot h_{mean} \cdot |\alpha \cdot T_c| \gg |\left(-\frac{B_c}{g} + A_c \right)| \cdot dt$. With the surface buoyancy and advective fluxes being negligible, and hence without an anomalous thermal or mechanical forcing, the mixed layer can only entrain water of the same density as that in the mixed layer, such that $M_n \cdot dt \approx (\rho_{mean} + \rho_n) \cdot h_n$, cancelling the corresponding term on the lefthand side of Eq. (4). Under these conditions, the temperature and salinity anomalies must compensate each other in their influence on density, allowing us, under these conditions, to estimate the salinity anomalies from the associated temperature anomalies.

The idea that such conditions exist is motivated by the observation that salinity changes are not only a response but can, in turn, constrain the drivers of density anomalies. Large freshwater anomalies, in particular, impede convection and entrainment (M) and thus limit the oceanic heat release to the atmosphere (B). At the same time, a stronger surface cooling is required to mix freshwater down, influencing the surface temperature (T).

To exploit this constraint of salinity on temperature, and identify these conditions, we derive indices that exhibit a strong relationship to subpolar temperature anomalies. We then take advantage of these relationships by regressing Eq. (4) onto the indices. Since the drivers are (by construction) not connected to the indices, they are likely to drop out after the regression such that the density changes implied by the temperature anomalies must be balanced by density changes associated with salinity anomalies. In essence, the indices serve as filters that detect the conditions c in which stratification has been controlled by salinity, allowing us, under these conditions, to infer the variability of freshwater from the SST.

3.2 Derivation of freshwater indices

To identify suitable indices for freshwater anomalies, we start with the NAO in summer (Fig. 1a), which has previously been linked to potential drivers of freshwater anomalies in the subpolar North Atlantic. On the one hand, a lower NAO phase in summer is associated with enhanced runoff and melting over Greenland (Hanna et al., 2013, 2021), which is a source of freshwater to the North Atlantic (Bamber et al., 2018; Dukhovskoy et al., 2019). On the other hand, a higher NAO phase is associated with an intensified subpolar gyre circulation, leading to enhanced freshwater imports into the subpolar region (Häkkinen et al., 2011a, 2013; Holliday et al., 2020). While the choice of the NAO index is motivated by these dynamical links, we here use it for a purely statistical purpose and make no assumptions on the dynamical underpinnings.
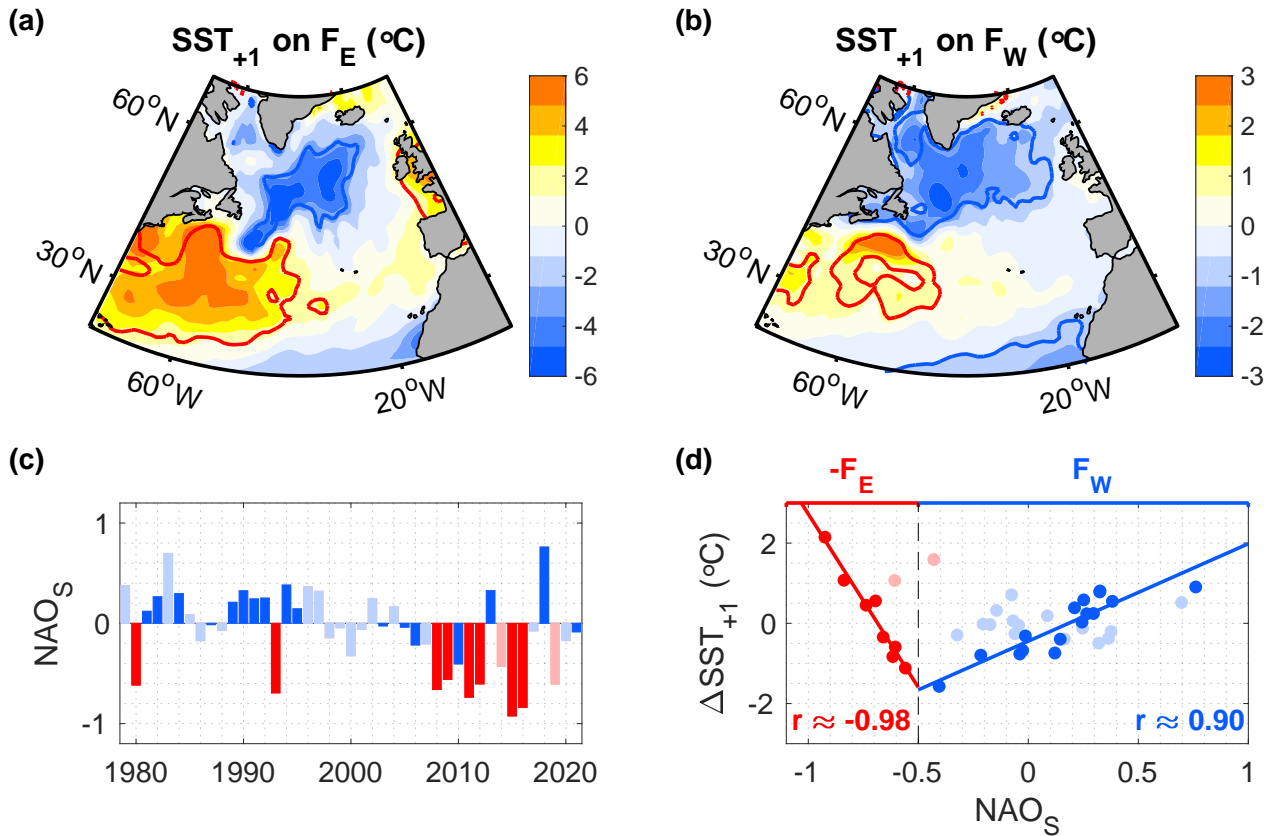
Figure 2. (a,b) Regression of the SST in winter (January through to March) onto two NAO$_S$ subsets below and above 0.5, where NAO$_S$ is the NAO index of the preceding summer (July and August). The corresponding years are shown by the strong red and blue colours in panels c and d, excluding the transparent years, which were selected to minimise the signal-to-noise ratio. Thus, F$_E$ includes 8 years while the regression on F$_W$ is based on 17 years. Contours encompass regions that are significant at the 95% confidence level. The '+1' in the title refers to the time lag of the SST signal since it appears in the winter after the summer index. Please note the different colour scales. (c) Variability of the NAO index in July and August (NAO$_S$), with the colour coding matching that in d. (d) Relationship between NAO$_S$ and the subsequent winter SST, where ΔSST corresponds to the SST difference between the red, subtropical and blue, subpolar 95% confidence regions in panels a (red years) and b (blue years) respectively, relative to the climatological mean.

Consistent with the existence of multiple possible drivers of freshwater and associated SST anomalies in winter, we obtain a qualitatively different relationship between the summer NAO index in July and August (NAO_S) and the meridional SST gradient across $\sim$45 °N in the subsequent winter below and above a threshold of ~ -0.5 in NAO_S. Below this threshold, there is a progressively larger SST difference between the northern subtropical region and the southern subpolar region for lower NAO_S states in the preceding summer. Above this threshold, there is a progressively larger SST difference for higher NAO_S states in the preceding summer (Fig. 2d, with the corresponding regions shown in Figure 2a and b and the corresponding years shown in Figure 2c).

To improve the capability of the identified subsets to filter out the conditions c that allow us to estimate freshwater anomalies from the temperature, we strengthen the relationships between the two NAO subsets and the meridional SST gradient through subsampling. The subsampling is motivated by the objective of achieving a steep regression slope between the subsampled NAO_S index and the subsequent SST anomaly, implying that small changes in the subsampled index correspond to large changes in the subsequent SST anomaly. In turn, this high sensitivity implies that the magnitude of the temperature term on the lefthand side of Eq. (4) becomes very large after regressing it onto the NAO subsets.

For the cold anomalies associated with lower states of the summer NAO, we select the years in which $NAO_S < -0.5$, excluding the outliers in 2014 and 2019. The threshold of ~ -0.5 and the outliers were identified through visual inspection of the relationship between the summer NAO and the meridional SST gradient in the subsequent winter (Fig. 2d). The resulting correlation of the selected subset with the SST difference between the warm subtropical warm and cold subpolar regions, enclosed within 95% confidence lines, is ~ -0.98 ($p \approx 2.8 \cdot 10^{-5}$). Here, we specifically selected the 95% confidence regions as a means to directly inspect the robustness of the correlations and ensure that they are not due to outliers or clusters. Another advantage of using spatial differences is that we filter out any potential, spatially uniform, radiative warming signals. However, the identified relationships are not sensitive to the exact regions.

For higher values of the preceding summer NAO state, the correlation with the subsequent SST gradient is weaker, amounting to $\sim$0.64 ($p \approx 0.001$). Thus, to optimise our method of inferring freshwater variations from Eq. (3), we select the years that most lead to an increase in the correlation and regression. Considering the trade-off between the number of years included and the resulting correlation, we selected $N = 17$ years as a reasonable compromise for obtaining a high correlation of $\sim$0.90 while keeping a relatively large sample size, reflected in low p-values ($p \approx 2.6 \cdot 10^{-6}$). However, the results are not sensitive to this choice.

Since the cold anomalies associated with higher NAO states extend over the western subpolar region, we refer to the selected years as 'F_W' subset. Thus, we distinguish these cold anomalies from those associated with the other subset, which we refer to as 'F_E' subset, for eastern subpolar cold anomalies (Fig. 2). Given their close relationships with the SST, the two subsets have optimal chances of describing the conditions c that allow to estimate freshwater anomalies from Eq. (4). While the choice of the subsets is thus motivated by their potential to represent freshwater anomalies, the focus of this study is on the link between freshwater anomalies and their downstream effects. The subsets are only used as a tool. High correlations between the subsets, the SST and, potentially, the associated freshwater anomalies are a prerequisite, not a conclusion, and we make no assumptions on the suitability of both subsets outside the selected years.

4 Results

Having selected two NAO subsets, we next assess their suitability for representing freshwater anomalies. Thus, we evaluate the associated mass balance, determine the accuracy of the obtained freshwater estimates and examine their links with European summer weather. To increase the robustness of the analyses, independent of the indices, we further construct composites of the ocean and atmospheric conditions associated with the 10 warmest and coldest European summers over the last 40 years and compare the preceding freshwater anomalies. Finally, we analyse the long-term variability of freshwater anomalies, estimate the role of ocean-atmosphere feedbacks, and discuss their implications for the predictability of European summer weather.

4.1 Estimation of freshwater anomalies

Taking advantage of the strong relationships between the selected NAO_S subsets and subsequent SST anomalies, we regress each term in Eq. (4) on the two subsets. We then evaluate the surface mass balance over the cold anomaly regions within the regions enclosed by the 95% confidence lines. When using different regions, for instance the full subpolar region where the SST anomaly is negative, the results do not change appreciably. In the following, we present the key analysis steps and results while a detailed evaluation and comparison with in-situ observations is provided in Appendix A.

First, we estimated the temperature term. Assuming that the mixed layers are relatively homogeneous, we approximate the mixed layer temperature with the SST. Even if the SST is slightly warmer or colder than the mixed layer temperature, the relationship between the mixed layer temperature and the mixed layer salinity still remains the same as that between the SST and the sea surface salinity, due to having a constant density profile in the mixed layer.

We then estimated the terms on the righthand side of Eq. (4), including the buoyancy fluxes, vertical Ekman transports and advection. Overall, we found: Regardless of which month is selected as starting month of the integration, the density increase implied by the cold anomalies associated with F_E and F_W is more than an order of magnitude larger than the density changes associated with A_n or B_n. Moreover, neither of these fluxes is significantly correlated with the subsets, and their spatial patterns are inconsistent with the obtained SST patterns (Appendix A).

With the buoyancy fluxes, vertical Ekman transports and horizontal advection being negligible, there cannot be an anomalous density flux through the base of the mixed layer. The mixed layer can only entrain water of the same density as that at the surface. Thus, M_n can only change the mixed layer depth, not the density. When integrated over the winter period, it can be approximated with $(\rho_{mean} + \rho_n) \cdot h_n$ canceling the corresponding term on the lefthand side of Eq. (4). We are left with $\rho_{mean} (-\alpha \cdot SST_n + \beta \cdot SSS_n) \cdot h_{mean} \approx 0$, where SSS is the sea surface salinity and n now refers to the anomalies obtained from the regressions.

With none of the terms on the righthand side of Eq. (4) being able to account for the the density increase, independent of the exact integration period, region, and mixed layer depth, we conclude that the density increase associated with the cold anomalies must be balanced by a density decrease associated with freshwater anomalies: $\alpha SST_E \approx \beta SSS_E$, and $\alpha SST_W \approx \beta SSS_W$. Physically, this density compensation implies that the freshwater anomaly determines the temperature that the surface water is required to have before it is mixed down.
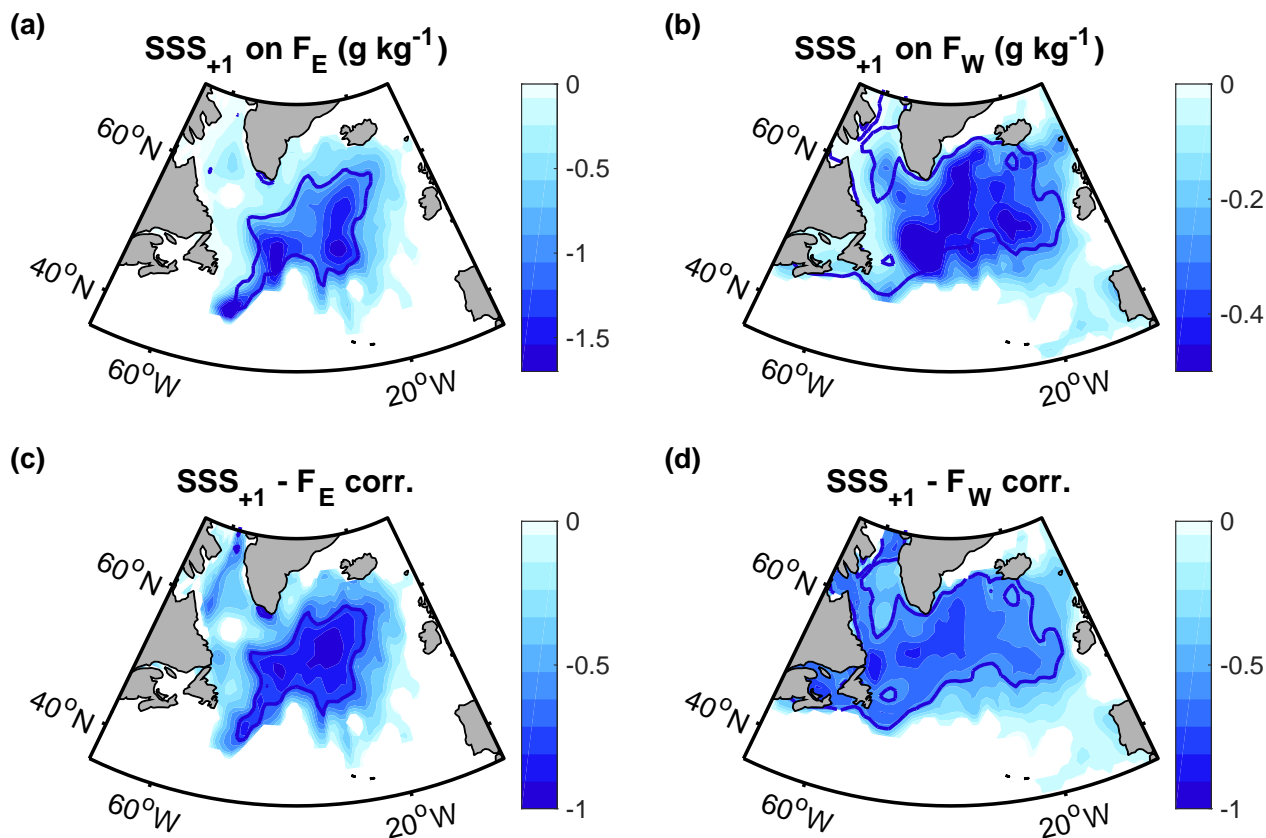
Figure 3. (a,b) Regression of the sea surface salinity in winter (January through to March) on the two freshwater indices from the preceding summer (Fig. 2). The contours delineate the regions that are significant at the 95% confidence level. (c,d) Correlations between the sea surface salinity in winter and the freshwater indices from the preceding summer, with the thick contours delineating the regions that are significant at the 95% confidence level, assessed by means of two-sided t-tests. The sea surface salinity has been estimated from the mass balance.

The estimated surface freshwater anomalies associated with F_E are strongest over the eastern subpolar region (Fig. 3a), while freshwater anomalies associated with F_W also extend over the western subpolar region (Fig. 3b). Since the buoyancy fluxes represent the largest term on the righthand side of Eq. (4), they determine the uncertainty of the obtained salinity estimates, amounting to 4% for the F_E subset and 7% for the F_W subset. Another advantage of the selected subsets is that they are, by construction, highly correlated with the obtained freshwater estimates in the subsequent winter, with the correlations exceeding 0.9 over large parts of the subpolar region (Fig. 3c and d).

Considering the low uncertainties of the obtained freshwater estimates, and their high correlations with the two NAO subsets, we conclude that both subsets represent suitable freshwater indices. This result implies a close connection between freshwater and SST anomalies. A demonstration of this connection with hydrographic observations shows that, even in winters with most intense air-sea fluxes, freshwater anomalies can be inferred from the SST with reasonably small uncertainties (Appendix A).

4.2 Causes of freshwater anomalies

The preceding derivation revealed two types of cold and fresh anomalies, which are associated with opposite atmospheric circulation patterns in the previous summer, characterised by high and low NAO states respectively. To better understand this nonlinear relationship between the NAO state in summer and the freshwater anomalies in the subsequent winter, we review potential large-scale drivers of the obtained freshwater anomalies.

Freshwater anomalies may result from enhanced sea ice or glacial melt, river runoff, surface fluxes (precipitation minus evaporation), and circulation changes. After investigating the surface fluxes from ERA5, glacial runoff from the Greenland climate model MAR, and the regional gyre circulation from altimetry, we find a significantly enhanced freshening in lower summer NAO states only for runoff (Fig. 4a). This is in agreement with earlier studies evaluating individual links between the summer atmospheric forcing, glacial runoff (Hanna et al., 2013, 2021), and the resulting freshwater input into the North Atlantic (Bamber et al., 2018; Dukhovskoy et al., 2019).

To further support the relationship between surface melting and subpolar freshwater anomalies we take advantage of the pronounced seasonality of the melting and runoff, being largest in summer (July and August). With the majority of the seasonal freshwater arriving in the subpolar gyre during autumn (Fratantoni and McCartney, 2010; Schmidt and Send, 2007), the surface mass balance has previously been evaluated for the period from summer to winter (Oltmanns et al., 2020). Thus, the summer NAO, multiplied by '−1' was identified as a suitable index for the seasonal freshwater that is newly added to the subpolar region in the subsequent autumn (Fig. 4b). The timing of the freshwater input, arriving between summer and winter, thus supports the role of seasonal runoff and melting for the identified freshwater anomalies.

While the full, un-subsampled summer NAO is a suitable indicator of the seasonal freshwater input from summer to winter, it is not necessarily correlated with the absolute surface freshwater anomaly in winter because smaller, seasonal freshwater anomalies are mixed down before a significant cold anomaly develops. Only when the seasonal freshwater release is sufficiently large does it lead to surface fresh and cold anomalies in winter (Fig. 2a and 3a). Otherwise, the SST and surface salinity in winter are increasingly influenced by other factors.

Among the dominant drivers of deeper freshwater anomalies is the subpolar gyre circulation. Specifically, a stronger subpolar gyre circulation has been found to lead to enhanced inflow of fresh and cold polar water from the coastal Labrador Current into the subpolar gyre (Häkkinen, 2002; Häkkinen and Rhines, 2009; Häkkinen et al., 2011a, 2013; Koul et al., 2020). Since the subpolar gyre circulation is, in turn, largely forced by the wind stress (Häkkinen et al., 2011b; Spall and Pickart, 2003), earlier studies have identified a significant link between a stronger wind stress curl over the subpolar North Atlantic and a reduced salinity in the subpolar gyre (Häkkinen and Rhines, 2009; Häkkinen et al., 2011a, 2013; Holliday et al., 2020).

Inspection of the absolute dynamic topography in winters after higher NAO states in summer confirms an intensified subpolar gyre circulation in the Labrador Sea (Fig. 4c), implying an enhanced geostrophic advection of cold and fresh polar water off the coast of Newfoundland into the subpolar region. This is expected as higher NAO phases imply an increased wind stress curl in the subpolar North Atlantic. After the subsampling, the signal becomes stronger (Fig. 4d), supporting the subsampling and the identified, increased freshwater correlations with a physical explanation.
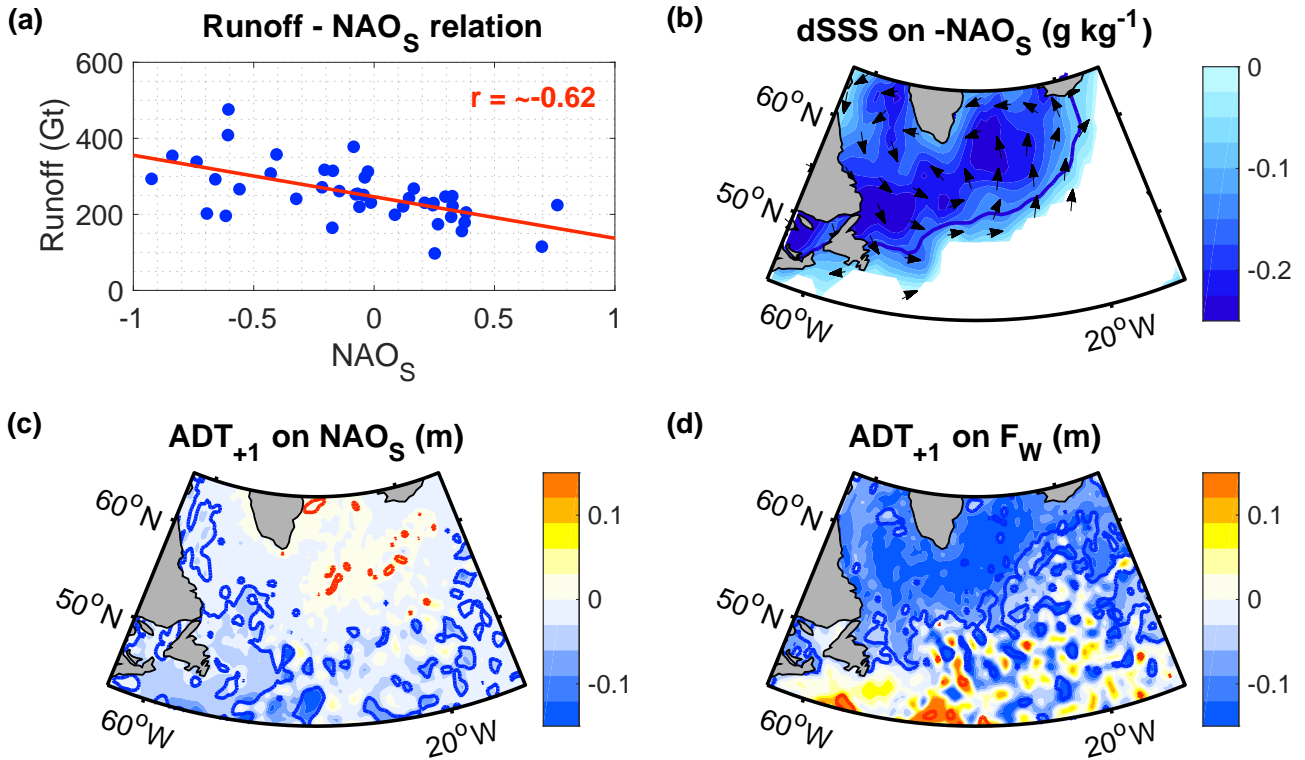
Figure 4. (a) Relationship between the NAO in July and August (NAO_S) and the total runoff integrated over the Greenland ice sheet, also in July and August. (b) Regression of the newly arriving, seasonal surface freshening from summer (August) to winter (January to March) onto $-NAO_S$ from the preceding summer. Multiplying the summer NAO by '-1' serves the purpose of obtaining an index that is positively correlated with the surface freshening. The seasonal surface freshening has been estimated from a surface mass balance (Oltmanns et al., 2020). (c,d) Regression of the absolute dynamic topography in winter (January to March) onto (c) NAO_S and (d) F_W from the preceding summer. Contours encompass regions that are significant at the 95% confidence level.

285   While a detailed quantification of freshwater budget is beyond the scope of this study, the proposed physical causes of the obtained freshwater estimates are supported by their spatial characteristics and intensities. F_W freshwater anomalies are largest over the western subpolar region, where the subpolar gyre circulation is strongest and where the surface heat fluxes are largest, mixing seasonal freshwater anomalies down. F_E freshwater anomalies are largest over the southeastern part of the subpolar region where surface fluxes and the gyre circulation are weaker, and where the mixed layer depths are shallower.
290 Consequently, freshwater anomalies associated with F_E are expected to be shallower and hence, more intense compared to freshwater anomalies associated with F_W, as they are distributed over a smaller depth range.

    We also examined the surface fluxes (precipitation minus evaporation) but found that they were too small to account for freshwater anomalies after both higher and lower NAO phases in summer. In autumn and winter, the surface freshwater fluxes

were evaluated as part of the buoyancy fluxes in the surface mass balance and found to be negligible. Moreover, on decadal timescales, freshwater releases in the subpolar region have been attributed to switches of the Arctic Beaufort gyre circulation (Proshutinsky et al., 2015). While these periodic, Arctic freshwater releases may have contributed to the low-frequency variability of the North Atlantic SST variability, we here focus on the higher-frequency variability of freshwater and the SST that is naturally extracted by subsampling the summer NAO.

Consistent with the observations and earlier studies, we conclude that, in most years (when $\text{NAO}_S \gtrsim -0.5$), the freshwater anomalies are responding to changes in the subpolar gyre circulation. In those years, the seasonal freshening is mixed down and too small to affect the absolute SST anomaly in winter. However, F_E freshwater anomalies have a higher sensitivity to the summer NAO than the F_W freshwater anomalies, which is reflected in steeper regressions (Figs. 2 and 3) and can be explained by shallower, seasonal mixed layers. As a result, freshwater anomalies, linked to enhanced seasonal melting, change faster with the summer NAO and at some point (when $\text{NAO}_S \lesssim -0.5$) become the dominant signal. The implication that seasonal runoff and melt can cause absolute freshwater anomalies in winter is new and suggests that many recent fresh and cold anomalies in the subpolar North Atlantic were forced by a different mechanism to those in earlier decades.

4.3 Atmosphere-ocean feedbacks in winter

Having identified two types of freshwater anomalies, we next examine their evolution in winter. We focus on the anomalies that are represented by the F_E subset (Fig. 3a) due to their sharper SST signals. However, freshwater anomalies associated with the F_W subset show qualitatively similar atmospheric responses, both in winter (not shown) and in summer (Section 4.4).

Since the meridional SST gradient is increased in winters after stronger freshwater anomalies, there is a sharper SST front between the subtropical and the subpolar gyre (Fig. 2a). Directly above this sharper SST front, we observe an amplified baroclinic instability in the atmosphere, indicated by an enhanced Eady growth rate (Fig. 5a).

The amplified baroclinic instability manifests itself in a distinct circulation anomaly. When an air parcel travels northward across the SST front, it rises because it is warmer than the surrounding air masses. By rising, the air column stretches, acquiring positive vorticity. The opposite occurs when an air parcel travels southward across the front. Consistent with the resulting enhanced baroclinic wave activity, the observations show a cyclonic anomaly to north of the SST front and an anticyclonic anomaly to the south (Fig. 5b), representative of a positive NAO phase. Thus, after strong F_E anomalies, the NAO anomaly switches sign. While a detailed investigation of the associated diagnostics is beyond the scope of this study, the observed atmospheric circulation anomalies are reproduced by SST-forced model simulations, albeit at lower amplitudes, supporting that the SST significantly contributes to these anomalies (Appendix B).

The obtained atmospheric circulation anomaly drives a convergent Ekman transport between the subtropical and subpolar gyre (Fig. 5b), leading to an increase in sea level. This Ekman transport is an instantaneous response but the resulting increase in sea level and horizontal pressure gradients can have longer lasting repercussions. Indeed, the increased sea level and associated ocean instabilities, manifest themselves in a broad band of anti-cyclonic eddies that extends into the second winter after the freshwater anomalies (Fig. 5c). The eddies are not visible in the SST due to the coarser 1° x 1° resolution of the SST product, compared to the 0.25° x 0.25° resolution of the absolute dynamic topography product.
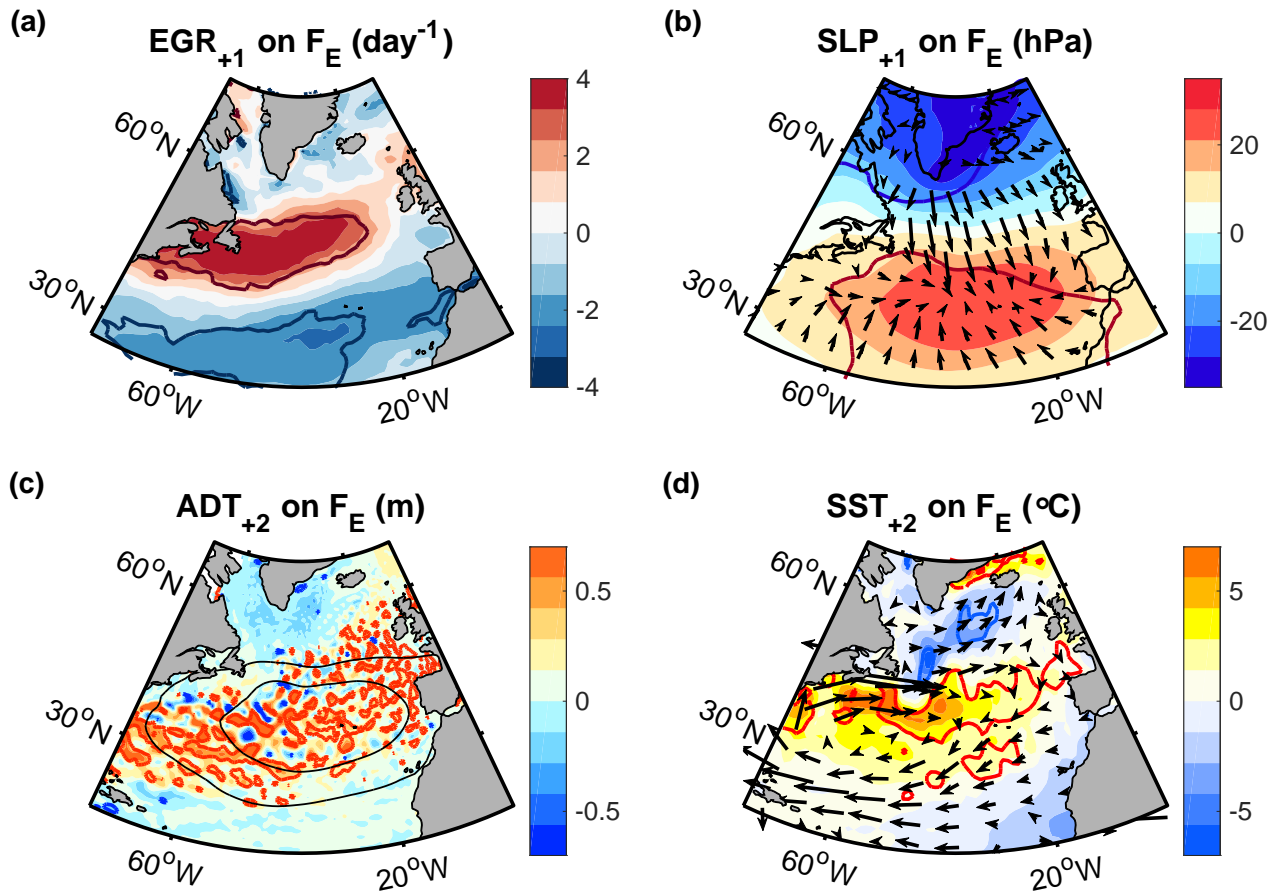
Figure 5. Regressions of (a) the maximum Eady growth rate, (b) the sea level pressure, (c) the absolute dynamic topography (ADT) and (d) the SST in winter (January through to March) on F_E. (a) and (b) are in the first winter after the anomalies whereas (c) and (d) are in the second winter after F_E (indicated by the '+1' and '+2' in the title). The arrows in (b) show the direction of the associated Ekman transports. The arrows in (d) represent the smoothed geostrophic flow implied by the ADT anomaly. The thin black contours in (c) show the region of Ekman flow convergence from (b). Thick contours in all panels encompass regions that are significant at the 95% level.

Considering that the mean flow along the eddies is eastward, representing the North Atlantic Current, the integrated effect of the anti-cyclonic eddies is a reduced eastward speed at the southern edge of the band and an increased eastward speed at the northern edge (Fig. 5d). This circulation pattern has been referred to as inter-gyre gyre circulation (Marshall et al., 2001) and is equivalent to a northward shift of the North Atlantic Current (Kostov et al., 2021; Zhao and Johns, 2014).

The northward shift of the North Atlantic Current implies a large-scale warm anomaly to the south of the subpolar cold anomaly, not because the water inside the current is anomalously warm but because the current occurs at an anomalously northward location. It is seen in the first, and the second winter after freshwater anomalies (Fig. 2a and 5d). However, in the first winter, the northward shift is obscured by the wind-driven, southward expansion of the cold anomaly over the eastern

North Atlantic, potentially driving enhanced mixing and erosion of the SST front. The spatial distribution of the surface heat fluxes, on the other hand, does not match the SST field (Fig. A1d), indicating that their influence may be limited.

We summarise that freshwater anomalies are linked to cold anomalies in the subpolar region in winter (Fig. 2). The cold anomalies contribute to an enhanced meridional SST gradient, implying a sharper SST front between the subpolar gyre and the subtropical gyre. The sharper SST front is associated with an amplified baroclinic instability in the atmosphere (Fig. 5a) that is characterised by a more cyclonic circulation anomaly over the subpolar gyre and a more anticyclonic anomaly to the south (Fig. 5b). This atmospheric circulation anomaly sets up pressure gradients, which in turn, drive a geostrophic flow that contributes to the warm anomaly to the south of the subpolar cold anomaly (Fig. 5c and d). The warm anomaly reinforces the SST anomalies, amplifying the air-sea feedback. While this mechanism has been demonstrated using the F_E subset, the signals for the F_W subset are qualitatively the same.

The overall effect of the air-sea coupling is an increased SST front between the subtropical warm anomaly and the subpolar cold anomaly, representative of the characteristic SST tripole pattern (Czaja and Frankignoul, 2002). The cold anomaly off the coast of western Africa can be explained by the large-scale atmospheric circulation anomaly over the subtropical region, leading to southward winds along the African coast and enhanced upwelling. Given the associated air-sea feedbacks, we do not causally attribute this large-scale SST signal to freshwater anomalies alone.

4.4 Implications for European summer weather

The preceding analysis revealed a close statistical link between freshwater anomalies and associated winter conditions. Next, we investigate the SST and atmospheric conditions in subsequent summers. In the first summer after stronger freshwater anomalies (again represented by F_E), we find that the SST is characterised by an enhanced meridional SST gradient with the subpolar cold anomaly covering part of the North Atlantic Current, as in the preceding winter (Fig. 6a). In the second summer, the northward shift of the North Atlantic Current is the most pronounced signal, implying that the region of the enhanced meridional SST gradient is shifted northward compared to the first summer (Fig. 6b).

As in the preceding winters, the SST fronts destabilise the overlying atmosphere, resulting in an enhanced jet stream along the front (Fig. 6a and b). In summer, moreover, there is an additional surface temperature gradient across the European coast, so the anticyclonic circulation anomaly is, in part rotated over the continent, and the jet stream is deflected northward (Fig. 6c and d). Thus, in line with the more northerly SST front and jet stream locations in the second compared to the first summer, we observe relatively warmer and drier air over southwest Europe in the first summer after stronger freshwater anomalies, and relatively warmer and drier air over northwest Europe in the second summer (Fig. 6e-h).

Freshwater anomalies associated with the F_W subset are also followed by a cold SST anomaly in the subsequent summer. However, compared to F_E freshwater anomalies, the cold SST anomaly after F_W freshwater anomalies is more confined in the central North Atlantic, with the regressions peaking in July and August (Fig. 7a). Consequently, we observe a sharp northward deflection of the jet stream (Fig. 7b), leading to more westerly warm and dry anomalies over Europe (Fig. 7c and d). While the warm anomalies after the F_E freshwater anomalies extend across the Iberian Peninsula all the way to northern Africa, the warm anomalies following the F_W freshwater anomalies are centred around over France and Great Britain.
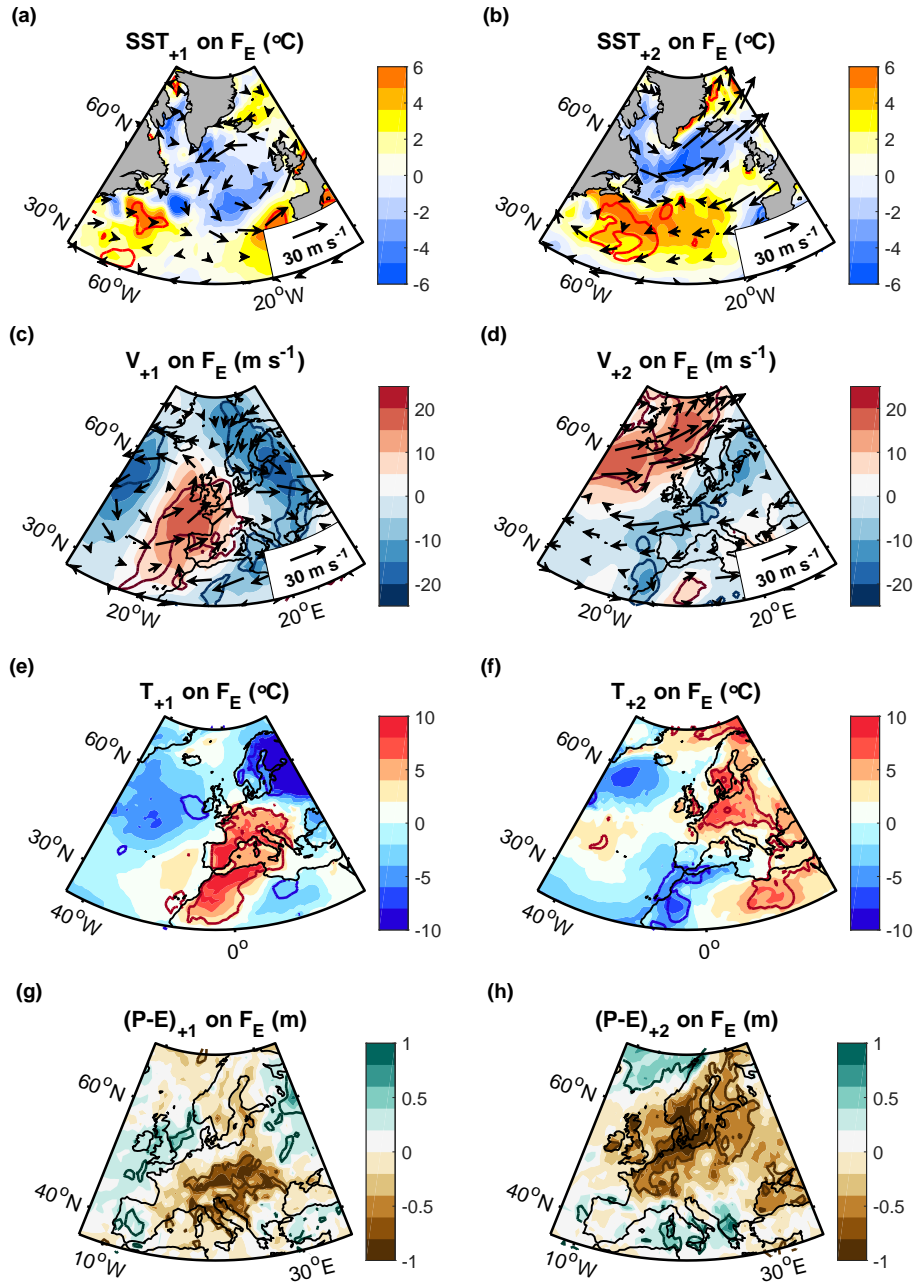
Figure 6. Regressions of (a,b) the SST with the 700-hPa winds, (c,d) the meridional winds at 700 hPa, (e,f) the 2-m air temperature and (g,h) the accumulated precipitation minus evaporation on F_E in (a,c,e,g) the first and (b,d,f,h) the second summer (May through August) after the freshwater anomalies (indicated by the '+1' and '+2' in the titles). We removed large-scale trends from the air temperature to reduce the direct warming effect of greenhouse gases (Section 2), and we excluded the anomaly in 2015 since its responses were covered by the 2016 anomaly (not shown). Thick contours encompass regions that are significant at the 95% confidence level.
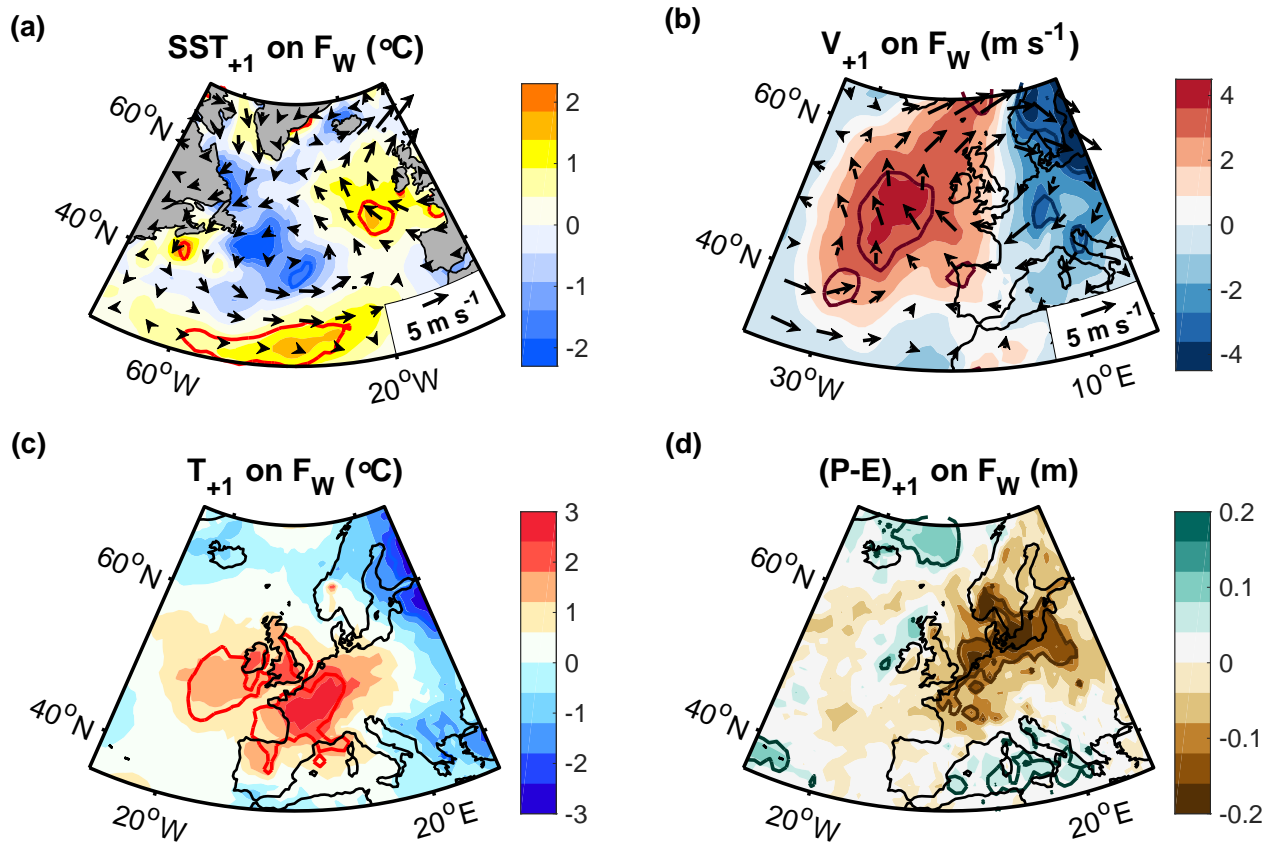
Figure 7. Regressions of (a) the SST with the 700-hPa winds, (b) the meridional winds at 700 hPa, (c) the 2-m air temperature and (d) the precipitation minus evaporation in summer (July and August) on F_W from the preceding summer, again after subtracting large-scale trends from the air temperature. The thick contours encompass regions that are significant at the 95% confidence level.

370   Moreover, the regressions of the SST and atmospheric circulation on F_W are weaker compared to those on F_E, consistent with weaker freshwater anomalies (Fig. 3) and smaller regression slopes (Fig. 2d). Physically, the higher regressions on the F_E subsets imply a higher sensitivity of the ocean and atmospheric conditions to F_E freshwater anomalies. Once the seasonal freshening exceeded a critical threshold (corresponding to a threshold of ~ -0.5 in the NAO_S index), a relatively small further increase was linked to substantially warmer and drier summers.

375   Despite these individual differences, the overall patterns are qualitatively similar after F_E and F_W freshwater anomalies: Both types of freshwater anomalies are characterised by a cold SST anomaly and northward deflection of the jet stream around the cold anomaly over the North Atlantic in the subsequent summer. In both cases, the northward deflection of the jet stream reduces the advection of moist, maritime air masses over different parts of Europe, resulting in warmer and drier weather.

4.5 Warm summers in Europe

The preceding analyses showed that two types of freshwater anomalies with opposite atmospheric drivers (characterised by a high and a low NAO states in the preceding summer) are followed by cold anomalies over the North Atlantic in winter, shifts in the jet stream and warmer, drier weather over Europe in the subsequent summers. Next, we investigate if warm European summers can, in turn, be linked back to a freshwater anomaly in the preceding year.

Based on composites, we find that the 10 warmest relative to the 10 coldest summers in Europe were associated with a pronounced cold anomaly over the North Atlantic, and an atmospheric circulation anomaly that is characterised by a northward deflection of the jet stream (Fig. 8a-e). Using a surface mass balance (Appendix A), we again trace the cold anomaly back to a freshwater anomaly in the preceding winter (Fig. 8f). Selecting different regions for the temperature variability over Europe shifts the location of the obtained anomalies but does not qualitatively alter these results.

This analysis of Europe's warmest and coldest summers supports the statistical link between freshwater anomalies and European summer weather. It demonstrates that the link is robust to the analysis technique and independent of the indices. While the regressions on the freshwater indices showed that freshwater anomalies can constrain the variability of the subsequent European summer weather, the composites additionally show that, on interannual timescales, Europe's largest temperature anomalies were preceded by freshwater anomalies. This indicates that enhanced freshwater anomalies are not only a sufficient but also a necessary condition for warmer European summers.

4.6 Variability of freshwater over the last 70 years

Next, we assess the longer-term variability of surface freshwater over the period since 1950. Following a surface mass balance analysis (Appendix A), we identify a significant freshwater trend accompanying a cooling trend in the subpolar region (Fig. 9a and b). The spatial SST pattern bears a high resemblance to the SST trend in summer (Fig. 9c), and the summer SST anomalies associated with increased runoff in the preceding year (Fig. 9d).

To investigate the variability of the SST pattern more closely, we project the SST variability each summer onto the pattern obtained from the SST trend. We use the region between $10° $ W, $65° $ W, $30° $ N and $60° $ N to focus on the area of reduced cooling (Fig. 9c and d). However the results are not sensitive to the exact region. Closer examination of the time evolution of the SST pattern reveals a high interannual variability, superimposed on the long-term trend (Fig. 9e and f). Moreover, the interannual variability of the SST pattern is significantly linked to the summer NAO and runoff from the preceding year. For instance, the correlation of the pattern with runoff is ~ 0.52 ($p \approx 3 \cdot 10^{-6}$), which remains significant after subtracting the trend ($r \approx 0.31$; $p \approx 0.01$).

Apart from seasonal runoff and melt-driven freshening, there are currently no conceivable, physical mechanisms in the tropics, stratosphere or outside the North Atlantic which, at the same time, have a significant trend over the last 70 years, exhibit a similarly high interannual variability, can explain the occurrence of freshwater anomalies in the subpolar region in the subsequent winter, and are significantly correlated with the characteristic summer SST pattern a year before it occurs. This suggests that seasonal freshening may not only be a predictor of the SST pattern but also a trigger, investigated next.
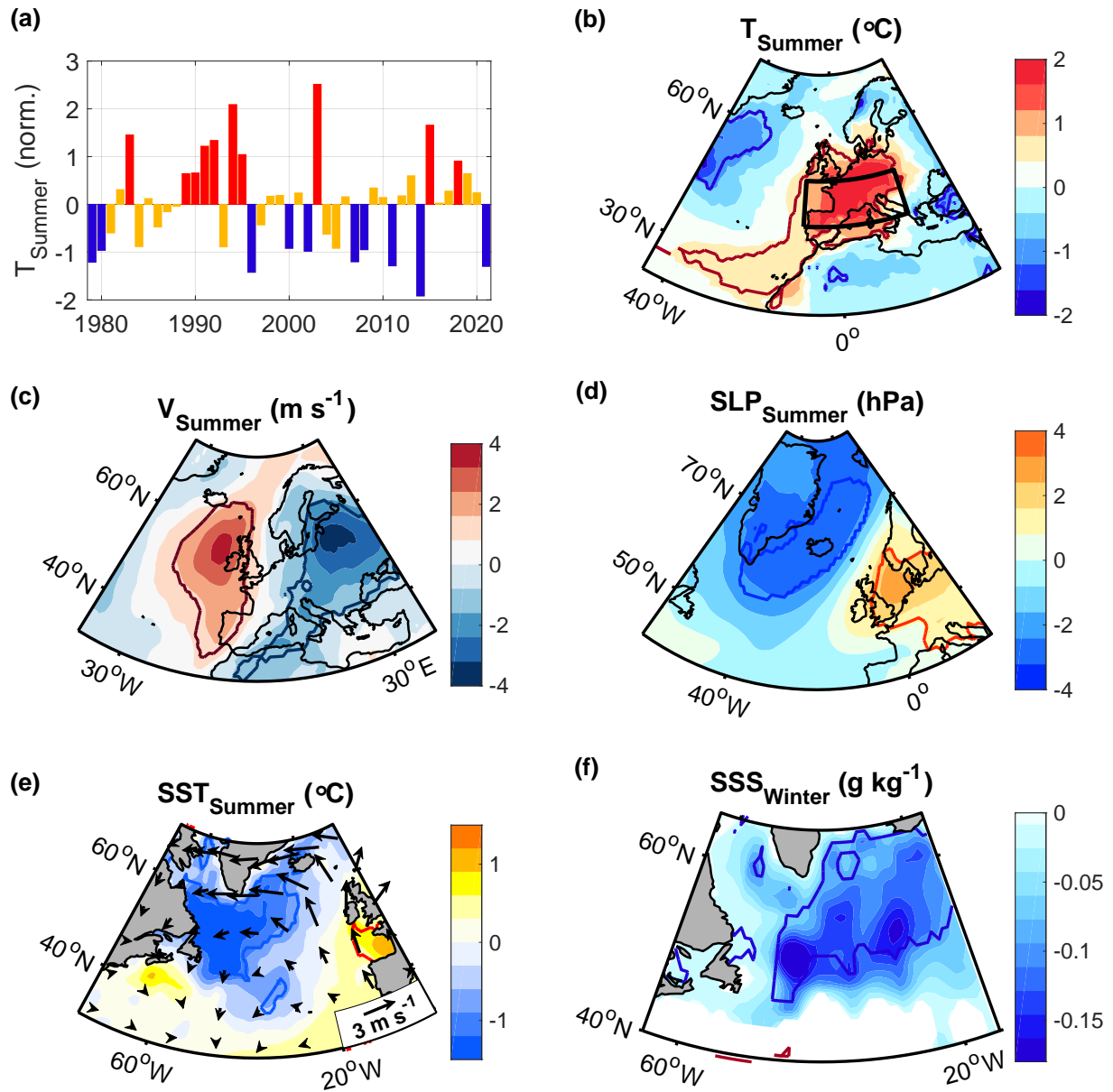
Figure 8. (a) Variability of the de-trended 2-m air temperature anomaly over land within the box shown in (b) during summer (July and August). (b,c,d,e) Composites of (b) the 2-m air temperature, (c) the meridional winds at 700 hPa, (d) the sea level pressure, and (e) the SST with the 700 hPa wind anomalies for the ten warmest minus the ten coldest summers, shown in (a). (f) Same as in (b-e) but for the sea surface salinity anomaly in the preceding winter, obtained from a surface mass balance (Appendix A). Contours delineate the regions that are significant at the 95% confidence level, assessed by means of two-sample t-tests.
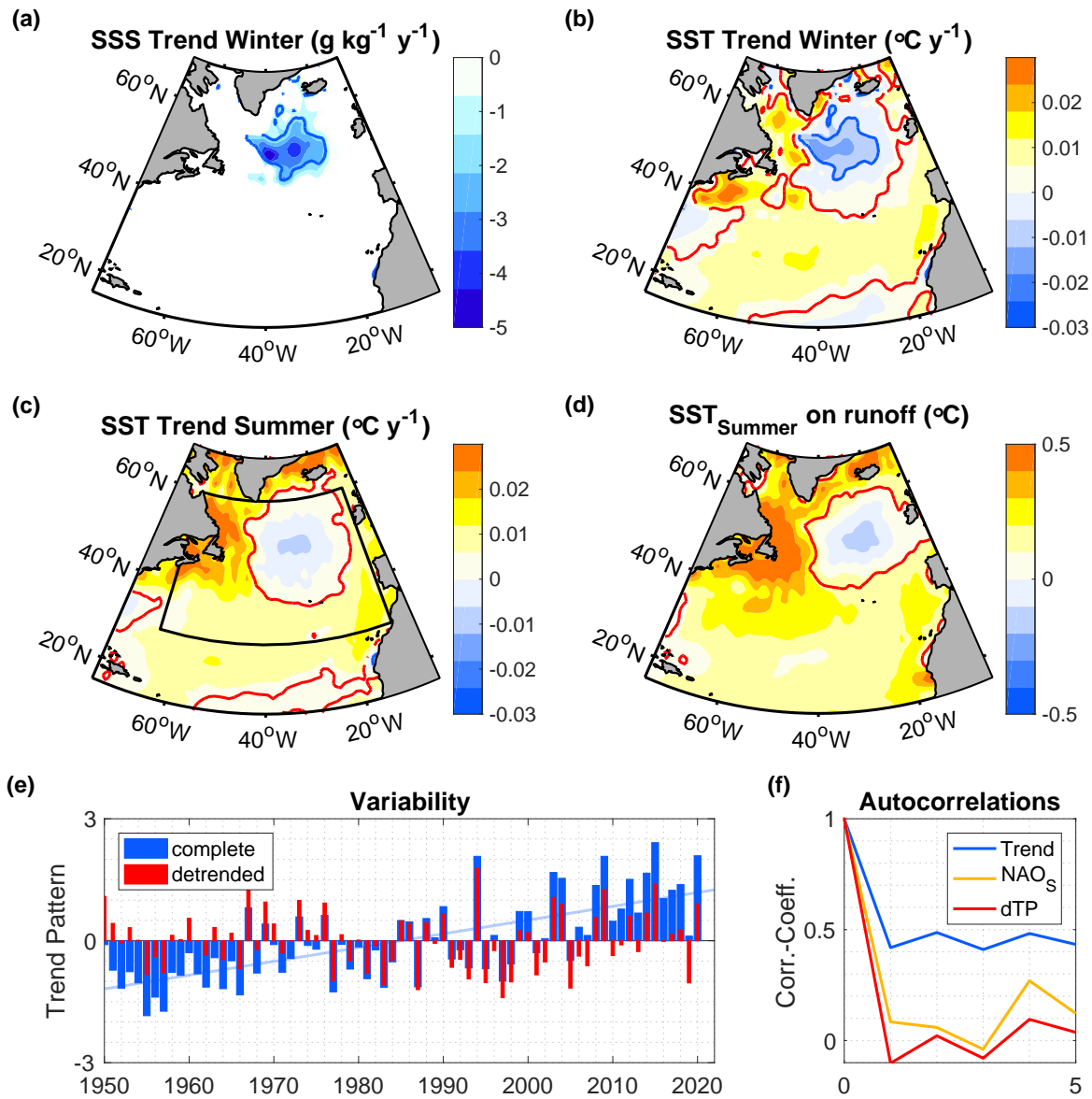
Figure 9. (a,b,c) Linear trend of (a) the SSS, obtained from a surface mass balance (Appendix A), and (b,c) the SST in winter (January to March) and summer (July and August) over the last 70 years. (d) Regression of the SST in summer onto the total (normalised) runoff from the preceding summer (July and August). Contours delineate the regions that are significant at the 95% confidence level. (e) Variability of the SST trend pattern in summer (blue bars) and the de-trended time series (red bars), obtained by (1) projecting the spatial variability of the SST in summer onto the trend pattern in (c) between $35°$ and $65°$ N and $10°$ and $70°$ W (shown by the box in c), and by (2) de-trending the resulting time series. (f) Autocorrelations of the time variability of the trend pattern (blue bars in e), the detrended time series (red bars in e) and the summer NAO in July and August.

4.7 Role of air-sea coupling

To assess the role of freshwater in triggering the SST signal, and thus, future implications of increased melting and runoff, we investigate the associated air-sea coupling processes. Therefore, we use the full, un-subsampled summer NAO as predictor. Using the summer NAO as predictor has the advantage that it occurs exactly one year before the summer SST pattern and European summer weather, has a high, interannual variability, a negligible trend and low autocorrelations. In addition, it is ubiquitously used, freely available, and does not include any processing. Still, we point that the subsequent results do not change appreciably if, instead of the summer NAO, we use runoff from the Greenland climate model MAR, or the variability of the SST trend pattern in summer (Fig. 9c).

Using the full, un-subsampled summer NAO as predictor, we find that, the cold anomaly one year after reduced NAO states in summer is associated with an enhanced atmospheric baroclinic instability across the European coastline and a cyclonic atmospheric circulation anomaly near the cold SST anomaly (Fig. 11a-c). This circulation anomaly is associated with a northward deflection of the jet stream along the European coastline and warmer, drier weather over parts of southern and southeastern Europe (Fig. 11d-f).

While a detailed heat budget of the mixed layers from winter to summer is beyond the scope of this study, we qualitatively examine the ocean and atmospheric processes, that may contribute to the SST development. Like in winter, we find that the surface heat fluxes have only a limited contribution to the subpolar cold anomaly and mostly in spring (Appendix C). However, the atmospheric circulation anomaly after lower NAO states in summer implies a more cyclonic wind field over the cold anomaly. This circulation anomaly leads to upwelling in the centre of the cyclone (Fig. 10) and thus increases the temperature contrast between the surface water, that is heated by solar radiation, and the deeper, upwelled water in the cyclone centre, that has been in contact with the atmosphere in the preceding winter and spring. Moreover, the warm anomaly region to the southeast of the cold anomaly region corresponds to a region of convergent Ekman transports and hence, downwelling (Fig. 10). The consistency of the SST signal with the regions of wind-driven up- and downwelling suggests that the atmospheric forcing may contribute to the development of the SST field.

The importance of the air-sea coupling is further supported by the evolution of SST signal, which intensifies from spring to summer and reaches its peak in July, when the temperature contrast between the upwelled water and the new summer water is largest. In addition, closer inspection of hydrographic observations from the cold anomaly region show that the hydrographic signal is relatively shallow, in line with the idea that it is forced by the atmosphere and contradicting the idea that it is caused, for instance, by a low-frequency change in the large-scale ocean circulation (Appendix C).

The previous analyses suggest that the atmospheric forcing and, specifically, the wind-driven transports play a key role in the development of the SST pattern. To assess, in turn, the role of the SST pattern in driving the atmospheric instability and warm and dry anomalies over Europe, we next define an SST index that captures the time variability of the cold anomaly pattern ('SST_{FW}'). For consistency with the observational analysis, we project the SST each summer onto the observed SST pattern after the summer NAO between $10°$ W, $65°$ W, $30°$ N and $60°$ N. However, selecting the SST trend pattern (Fig. 9c), or the pattern obtained from runoff (Fig. 9d), yields qualitatively the same results.
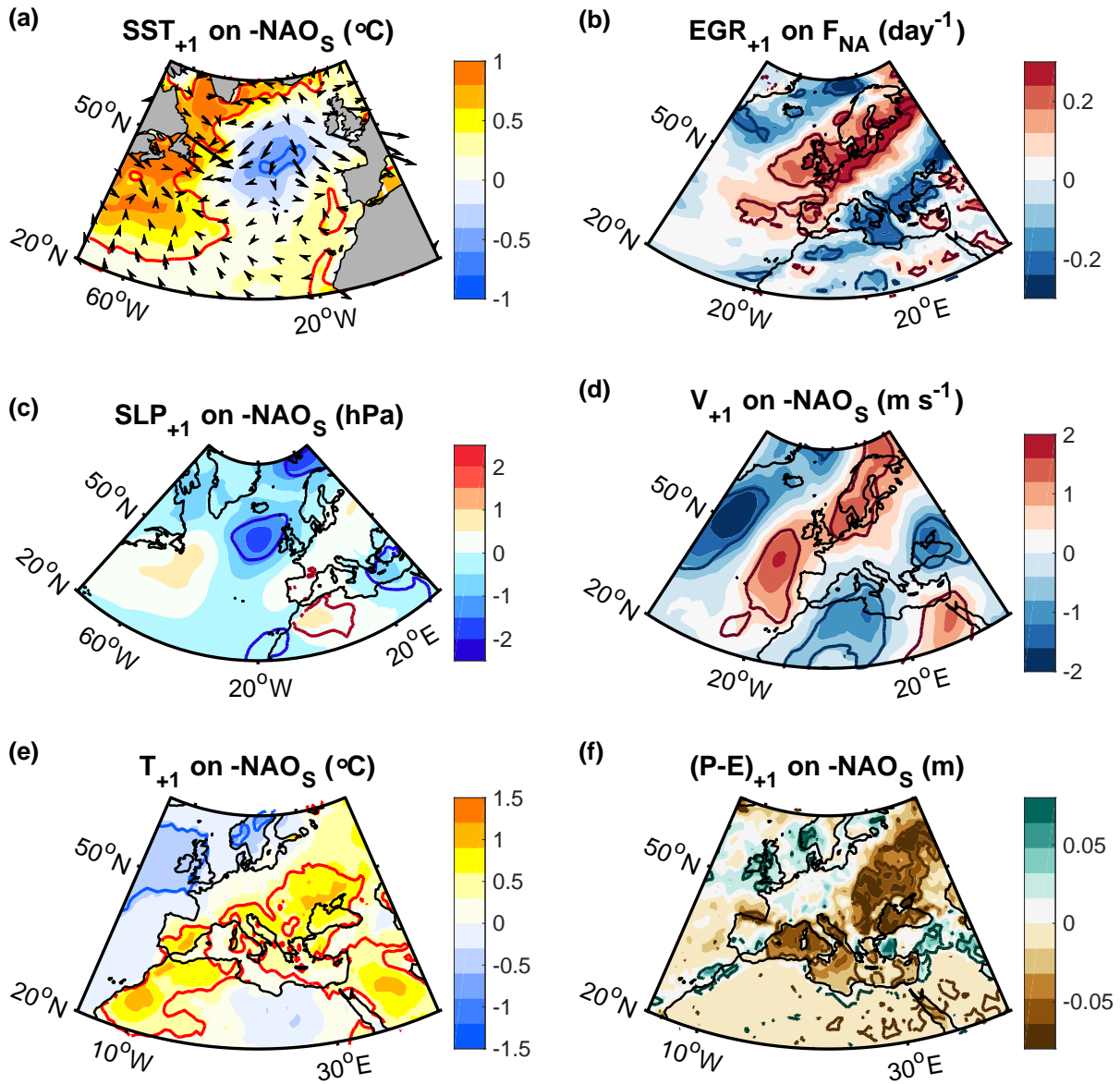
Figure 10. Regression of (a) the SST, with arrows indicating the direction of the Ekman transports, (b) the maximum Eady growth rate, (c) the sea level pressure, (d) the meridional component of the winds at 700 hPa, (e) the 2-m air temperature, and (f) precipitation minus evaporation from May through to August onto $-\mathrm{NAO}_S$ in July and August from the preceding year. Again, we subtracted the large-scale trends from the air temperatures. Contours delineate the regions that are significant at the 95% confidence level.
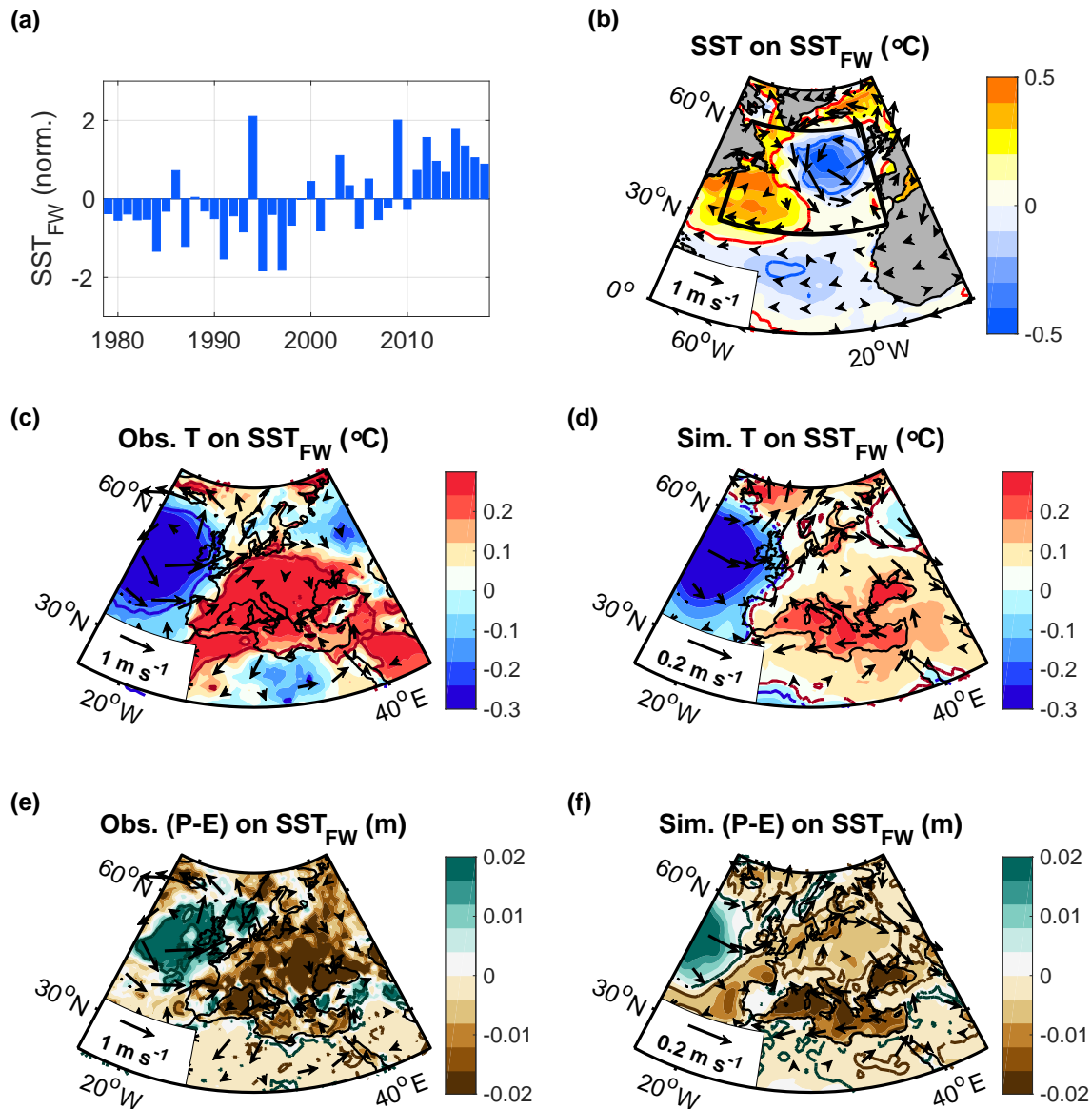
Figure 11. (a) Variability and (b) distribution of the SST pattern one year after the summer NAO, obtained by projecting the SST pattern in the box in (b) each summer (May through August) on that after the summer NAO (Fig. 10a). (c,d,e,f) Regressions of (c,e) the observed and (d,f) simulated 2-m air temperature and precipitation minus evaporation in summer onto the normalised SST_{FW} index, again after subtracting the large-scale trend from the air temperature. The simulations were acquired from 50 ensemble simulations from ECHAM5 and 40 ensemble simulations from CAM5 over the period 1979–2018, performed with the pre-scribed, observed SST. Shown is the mean of the regressions from the ensemble members, not the regression of the mean. Arrows indicate the observed and simulated 700 hPa winds respectively. The thick contours encompass regions that are significant at the 95% confidence level.

Next, we regress the temperature and precipitation anomalies, obtained from 90 ensemble simulations over 40 years, performed with prescribed observation-based SSTs, onto this newly-defined SST_{FW} index (Fig. 11a and b). We obtain a significant link between the prescribed SST pattern and the temperature and precipitation anomalies over Europe, both in the observations (Fig. 11c and e) and in the simulations (Fig. 11d and f). Overall, the observed and simulated atmospheric responses agree qualitatively well but the simulated responses are weaker and cover a larger area (Fig. 11c-f). We attribute this underestimation of the obtained atmospheric anomalies in the simulations to potential model biases (Osborne et al., 2020) and the lack of air-sea coupling.

We conclude that the atmospheric forcing contributes to the development of the SST field but is in turn, forced by it. On the one hand, the consistency of the spatial SST pattern with the wind-driven transports, the intensification of the SST signal in mid-summer, and the vertical extent of the hydrographic anomaly point to the relevance of the atmospheric forcing in driving the SST signal over the North Atlantic. On the other hand, model simulations, forced with the prescribed, observed SST, reveal the importance of the SST field for the large-scale atmospheric circulation, including for European summer weather. The underlying SST pattern covers the entire North Atlantic with the strongest signal occurring in the subpolar region (Fig. 11b). While further studies are necessary to confirm the dynamical contribution of freshwater anomalies to the large-scale SST pattern, its spatial and temporal characteristics, and the time lag of one year, indicate that enhanced surface freshening from the preceding year may have initiated the chain of air-sea feedbacks.

4.8 Predictability of European summer weather

The preceding analyses revealed significant links between North Atlantic freshwater anomalies and European summer weather in subsequent years. This raises the question to what extent this link can be exploited to predict European summer weather in advance. Thus, in this last analysis, we assess the predictability based on the explained variance in the observations, estimated by means of the squared correlation coefficient with the freshwater indices.

The variance of the near surface temperature and precipitation minus evaporation anomalies, explained by the F_E subset, reaches and even exceeds 80% over large parts of Europe (Fig. 12a-d). For the F_W subset, the explained variance drops to $\sim$50% (Fig. 12e and f), as expected from the reduced correlation between the F_W index and the corresponding freshwater anomalies. In both cases, the explained variance is largest in the regions that show the strongest links with the temperature and precipitation minus evaporation anomalies (Figs. 6 and 7). Given the high interannual variability of European summer weather and the summer NAO, reflected in low autocorrelations, we do not expect these explained variance to be significantly affected by a long-term trend.

A disadvantage of estimating predictability from the freshwater indices is the small sample size. If, instead, we approximate the freshwater variability by the meridional SST gradient in winter as an alternative freshwater index that covers the full period of investigation (Fig. 2d), or if we replace it by the full, un-subsampled summer NAO to only represent the contribution from the seasonal runoff- or melt-driven freshening component, the explained variance of European summer weather decreases to $\sim$20% and extends over a broader area (not shown).

Overall, we find: The higher the correlation is between the initial freshwater anomaly and its index, the higher is also the variance of European summer weather that the index subsequently explains. The F_E index, in particular, has an extremely high correlation with the initial freshwater anomaly of over $\sim$0.9 (Fig. 3c) and explains over 80% of the variance of European summer weather. Notwithstanding the small sample sizes, these results indicate that accurate observations of surface freshwater in the subpolar region can serve as valuable constraints for seasonal to interannual weather forecasts.

In addition, the nonlinear relationship between the summer NAO and European summer weather indicates that, once seasonal freshwater is not mixed down, corresponding to a threshold of $\sim$0.5 in the summer NAO, the sensitivity of European summer weather to seasonal melting rapidly increases. While this rapid increase in predictability provides new opportunities, the higher sensitivity also raises caution that a further increase in seasonal melting and runoff may lead to a more frequent crossing of the critical freshwater threshold and initiate a chain of feedbacks with substantial effects on European summer weather.

5 Conclusions

In this study, we examined the link between North Atlantic freshwater anomalies and European weather in subsequent summers. Given the limitations of currently available salinity observations, we derived two freshwater indices that were highly correlated with subpolar freshwater anomalies. Taking advantage of the high correlations both indices were used to detect links between the freshwater anomalies, the subsequent ocean-atmosphere evolution, and European summer weather. We further supported the identified links by starting from European summer weather and examining its relation to preceding freshwater anomalies. Lastly, we investigated the freshening trend over the last 70 years, the associated ocean-atmosphere feedbacks and their implications for European summer weather.

The analyses jointly reveal that enhanced freshwater anomalies are associated with subpolar cold anomalies and an increased meridional SST gradient in winter. The increased meridional SST gradient is linked to an amplified atmospheric instability and a large-scale atmospheric circulation anomaly with a more cyclonic circulation over the subpolar region and an anticyclonic anomaly to the south. This atmospheric circulation anomaly induces a northward shift in the North Atlantic Current which contributes to a warm anomaly to the south of the subpolar cold anomaly, amplifying the meridional SST gradient. In subsequent summers, the jet stream is deflected northward over the North Atlantic, aligned with the underlying SST fronts, leading to warmer and drier weather over Europe.

The observed evolution of freshwater anomalies follows the chain of events predicted by theory. Specifically, the link between freshwater and cold anomalies is constrained by conservation of mass. The subpolar cold anomaly increases the meridional SST gradient leading to an increased meridional temperature gradient which promotes an amplified baroclinic instability (Eady, 1949; Davies and Bishop, 1994). Moreover, the ocean's response to the resulting atmospheric circulation is expected from Ekman transports and geostrophy (Munk, 1950; Stommel, 1948; Vallis, 2017). These theoretical underpinnings support the identified statistical relationships and point to a coherent, deterministic mechanism that links North Atlantic freshwater anomalies to European summer weather.
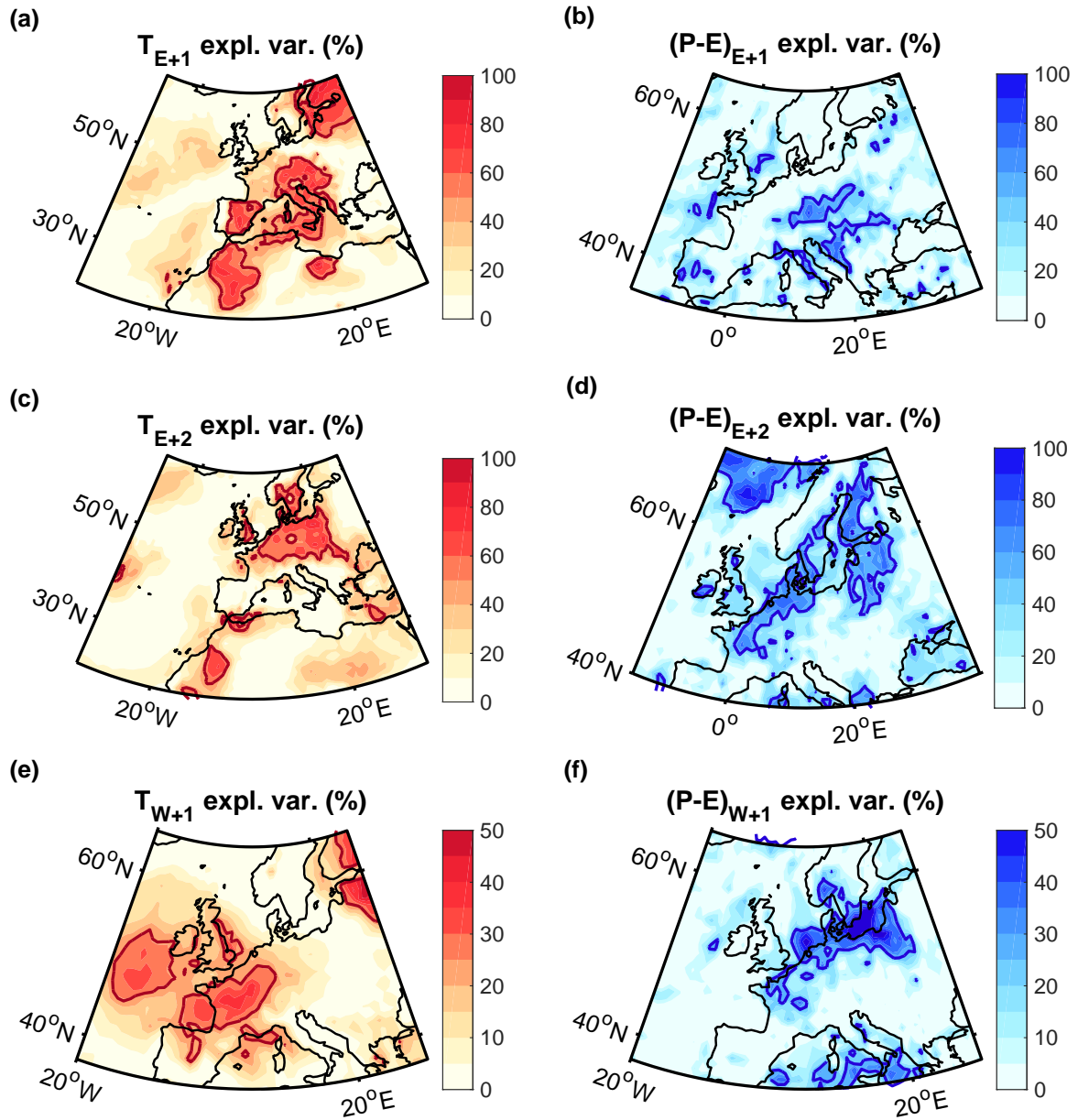
Figure 12. Variances explained by (a-d) F_E and (e,f) F_W of (a,c,e) the 2-m air temperature and (b,d,f) precipitation minus evaporation after freshwater anomalies. '+1' and '+2' in the titles refer to the first and second summer after the NAO subsets. Thick contours delineate the regions, in which the correlation is significant at the 95% confidence level, assessed by means of two-sided Student t-tests. The explained variances were obtained from the squared correlation coefficients. Please note the different colour scales.

Notwithstanding the importance of freshwater as a useful predictor of European summer weather, the evolution and intensification of the associated SST patterns through winter and summer can only be explained by a chain of ocean-atmosphere feedbacks. Further studies are needed to quantify the relative contributions of different drivers and their uncertainties, and the role of freshwater as potential trigger of the feedback chain. To date, no conceivable alternative trigger in the tropics, stratosphere or outside the North Atlantic region can explain the high-frequency, interannual variability, the trend, the spatial characteristics of the SST signal, its relationship with the summer NAO and runoff and hence, the initiation of the feedback chain a full year before the European summer weather as convincingly as freshwater.

Current numerical weather prediction systems show very limited to no forecast skill for European summer weather (Arribas et al., 2011; Dunstone et al., 2018). Thus, the existence of a link between North Atlantic freshwater anomalies and European summer weather indicates new potential to enhance the predictability of European summer weather a year in advance. Further studies that improve the representation of North Atlantic freshwater variations in models, and that quantify the predictability arising from them, are therefore desirable. In addition, targeted observational networks that monitor the variability of freshwater anomalies may help improve current forecast systems and circumvent the use of indices in future.

The melting of ice and runoff are expected to further increase in the coming decades (Notz and Stroeve, 2018; Briner et al., 2020), resulting in an enhanced freshwater discharge into the North Atlantic. With stronger freshwater anomalies, our results indicate a rapid increase in the risk of warm, dry European summers and of heat waves and droughts accordingly. Unfortunately, global climate models have difficulties in capturing the hydrographic structure in the subpolar North Atlantic, including the distribution of freshwater (Menary et al., 2015; Heuzé, 2017; Liu et al., 2017; Sgubin et al., 2017; Mecking et al., 2017; Wu et al., 2018). Considering the identified links between freshwater anomalies and the subsequent ocean and atmospheric evolution, our results suggest that models may miss a key source of climate variability and potential long-range predictability.

Code and data availability. This study is only based on publicly available data and standard analysis techniques. The SST and NAO data are available from NOAA (https://psl.noaa.gov/data/gridded/data.noaa.oisst.v2.html and https://www.cpc.ncep.noaa.gov/products/precip/CWlink/pna/nao.shtml). The Hadley SST data is available from https://www.metoffice.gov.uk/hadobs/hadisst/ and a complete merged NOAA and Hadley SST product can be obtained from https://gdex.ucar.edu/dataset/158_asphilli.html. Absolute dynamic topography data is distributed by the Copernicus Marine Environment Monitoring Service (https://marine.copernicus.eu/). ERA5 data can be obtained from the European Centre for Medium-Range Weather Forecasts (https://www.ecmwf.int/en/forecasts/datasets/reanalysis-datasets/era5) and the ECHAM5 and CAM5 model output can be downloaded from the Facility of Climate Assessments repository (https://psl.noaa.gov/repository/facts). Matlab codes can be obtained from the corresponding author.

Appendix A: Mass balance analyses

540   The following sections include the evaluation of the mass balances obtained from the freshwater indices (A1), those obtained from the SST composite and trend (A2), and a demonstration of the mass balance with hydrographic observations (A3).

A1   Surface mass balance for freshwater indices

Taking advantage of the strong relationships between the NAO_S subsets and subsequent SST anomalies, we regress each term in Eq. (4) onto the indices and evaluate the surface mass balance over the subpolar cold anomaly regions within the 95%
545   confidence lines (Figs. A1a and A2a).

    Considering that mean mixed layer deepens from summer to winter, reaching its maximum in late winter, the integrated anomalies in the surface heat and buoyancy fluxes during autumn are predominantly driven by existing anomalies in the density profile. For instance, an anomalously warm and light layer of water will lead to increased ocean heat and buoyancy losses once it has been entrained (Timlin et al., 2002). Thus, given that the anomalies in B_n and M_n are expected to largely
550   compensate for each other when integrated over autumn (the period of rapid mixed layer deepening), we focussed on the winter period (January through to March), when the amplitude and variability of the surface fluxes is largest. However, if we integrate the terms on the righthand side of Eq. (4) over autumn and winter, instead of only winter, the magnitude of the integrated anomalies does not appreciably change and their signs remain the same.

    First, we estimate the horizontal transports A. On the timescales and spatial scales considered, the strongest horizontal
555   velocities result from the geostrophic surface flow (including eddies and the subpolar gyre circulation). These surface flows do not contribute to a net mass increase as they occur along lines of constant density and pressure. The largest ageostrophic surface flow in the open ocean results from the wind forcing, which we evaluate using the wind stresses from the atmospheric reanalysis ERA5. Integrated over the winter period (January through to March), we find that neither the horizontal Ekman transports nor the vertical Ekman pumping can account for the density increase associated with the cold anomaly. They are not
560   significantly correlated with the freshwater indices, their amplitudes are too small, and their directions are inconsistent with the cold anomaly (Figs. A1a, b and A2a, b).

    Next, we estimate the buoyancy flux anomalies $B = \frac{g\alpha}{c_p}Q + g\beta S(P - E)$, where c_p is the heat capacity, Q is the heat flux (positive downward) and $P - E$ is the freshwater flux in kg m^{-2} s^{-1} (Gill, 2016). After evaluating the buoyancy fluxes with 6-hourly ERA5 output and regressing them on the freshwater indices, we find that they do not match the distribution of the
565   SST (Figs. A1c and A2c). The surface heat fluxes, which have the largest contribution to the buoyancy fluxes, are also not significantly correlated with the indices (Figs. A1d and A2d). When averaged over the cold anomaly regions, enclosed by the 95% confidence lines, and integrated over the winter, the buoyancy flux anomaly associated with the F_E subset reflects an anomalous mass decrease of $\sim$7 kg m^{-2} whereas the cold anomaly implies a mass increase of $\sim$204 kg m^{-2}. Likewise, the buoyancy flux anomaly associated with the F_W subset reflects a mass decrease of $\sim$5 kg m^{-2}, whereas the cold anomaly
570   implies a mass increase of $\sim$74 kg m^{-2}.
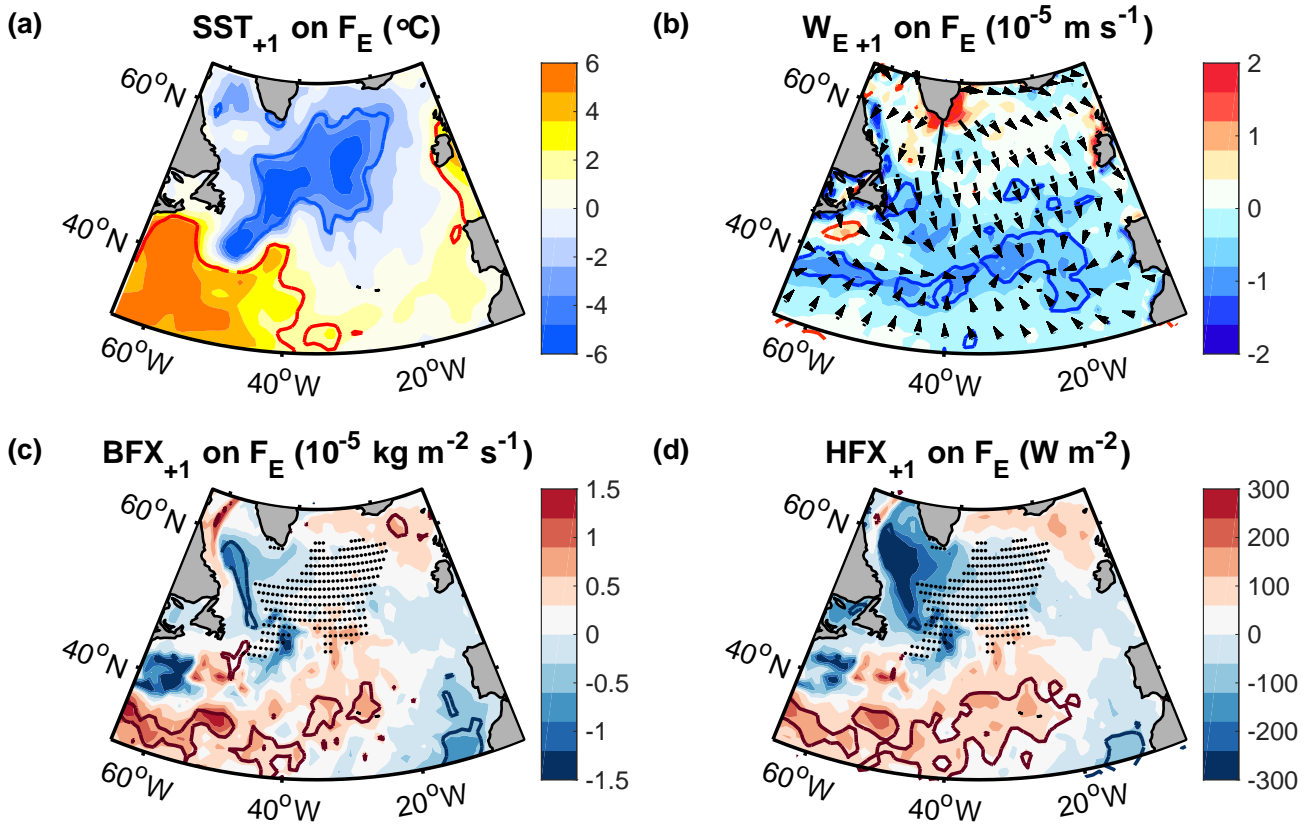
Figure A1. Regression of (a) the SST, (b) the vertical Ekman velocity (positive upward), (c) the buoyancy flux anomaly (positive downward) and (d) the surface heat fluxes (also positive downward) in winter (January through March) on F_E from the preceding summer. The arrows in (b) indicate the direction of the horizontal Ekman transports and the dots in (c) and (d) show the region used for the mass balance calculations, corresponding to the cold anomaly region. Contours encompass regions that are significant at the 95% confidence level.

With the buoyancy fluxes, vertical Ekman transports and horizontal advection being negligible, there cannot be an anomalous density flux through the base of the mixed layer. The mixed layer can only entrain water of the same density as that at the surface (Section 4.1). If anomalously cold water from below is entrained, it must also be anomalously fresh. Thus, it drops out of Eq. (4).

575   Since none of the potential drivers of density anomalies on the righthand side of Eq. (4) can account for the density increase associated with the cold anomalies, we conclude that the density increase associated with the cold anomalies must be balanced by a density decrease associated with freshwater anomalies. The buoyancy fluxes represent by far the largest term on the righthand side of Eq. (4), and thus determine the uncertainty of the obtained salinity estimates, amounting to ∼4% for the F_E subset and ∼7% for the F_W subset.
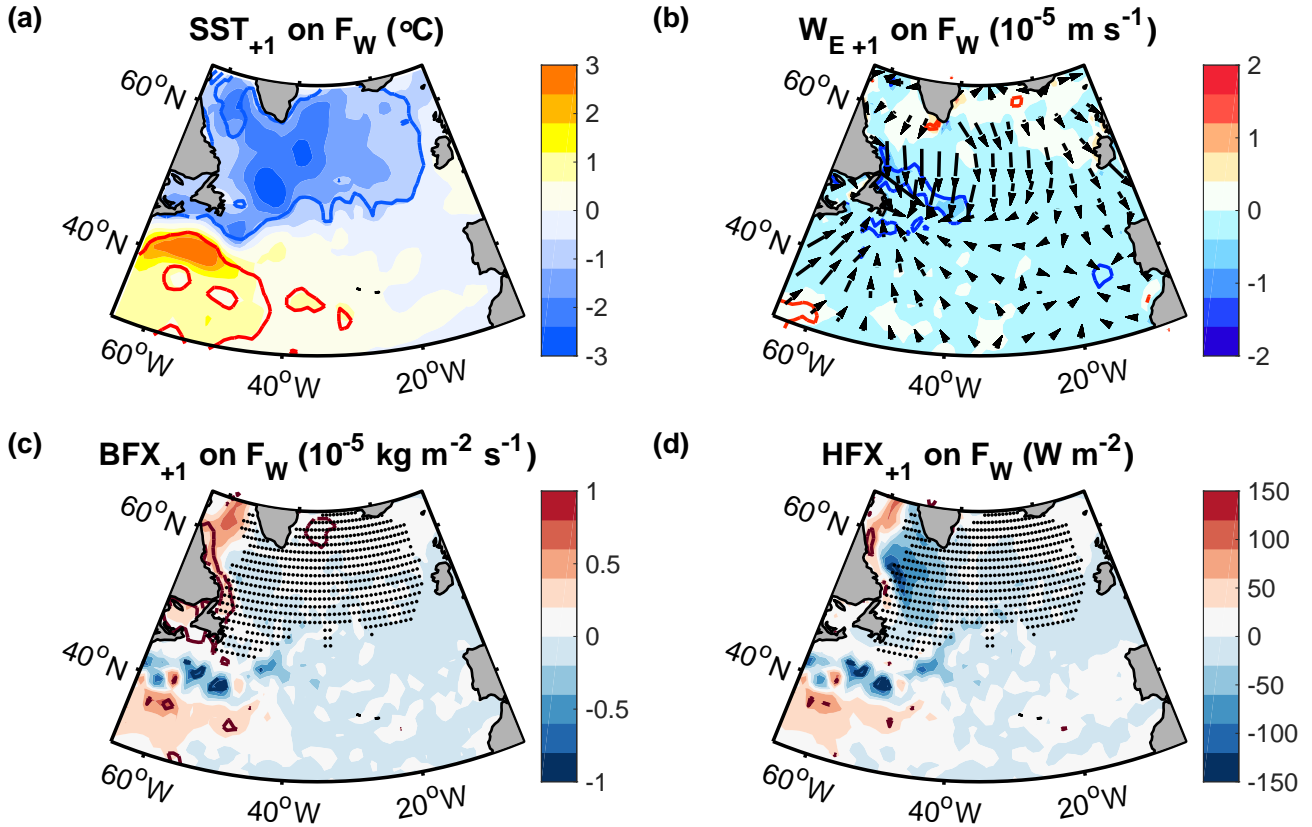
Figure A2. Regression of (a) the SST, (b) the vertical Ekman velocity (positive upward), (c) the buoyancy flux anomaly (positive downward) and (d) the surface heat fluxes (also positive downward) in winter (January through March) on F_W from the preceding summer. The arrows in (b) indicate the direction of the horizontal Ekman transports and the dots in (c) and (d) show the region used for the mass balance calculations. Contours encompass regions that are significant at the 95% confidence level.

580   In the calculations, we used a mean density of $\rho_{mean} \approx 1000$ kg m^{-3}, and a climatological mean winter mixed layer depth h_{mean} of ~250 m and ~280 m in the F_E and F_W cold anomaly regions respectively, obtained from Argo float profiles (Holte et al., 2017). While the results are not sensitive to these values, the positive correlation of density and mixed layer depth anomalies can lead to an underestimate (but not overestimate) of the freshwater anomalies, due to the involved nonlinearity in the regressions.

585   To verify the robustness of the results, we tested different integration periods and regions for the mass balance calculations. For instance, we also integrated the transports and surface fluxes from September to March instead of January to March, and we extended the investigated region over the full cold anomaly region, over which the SST anomaly is negative. In each case, the results did not change appreciably.

A2 Surface mass balance of the SST composite and trend

590 We further carried out a mass balance analysis for the composites of the cold anomaly in the winters preceding the 10 warmest relative to the 10 coldest summers over Europe (Fig. 8). Thus, we again evaluated the terms in Eq. (4) over the cold anomaly region and the winter, where now, the subscript n refers to anomalies associated with the composites.

After evaluating the terms in the mass balance equation, we obtain similar patterns compared to those associated with the two NAO subsets (not shown). Again, we find that none of the density drivers on the righthand side of Eq. (4) show a significant

595 signal over the cold anomaly region, and their amplitudes cannot account for the density increase implied by the cold anomaly. The surface buoyancy flux, which is the largest term on the righthand side of Eq. (4), amounts to $\sim +1.3$ g kg^{-1} while the density anomaly implied by the cold anomaly is ~ -40 g kg^{-1}. Thus, the uncertainty of the estimated freshwater anomaly (Fig. 8e) is $\sim 3\%$.

Lastly, we performed the surface mass balance analysis for the SST trend over the last 70 years (Fig. A3). When averaged

600 over the cold anomaly region, enclosed by the 95% confidence lines, the density increase implied by the cold anomaly amounts to ~ -0.42 kg m^{-2}. The terms on the righthand side of the mass equation are negligible, except for the surface buoyancy fluxes, which amount to $\sim +0.048$ kg m^{-2}, implying an uncertainty of $\sim 11\%$ for the estimated freshwater anomaly (Fig. 9a).
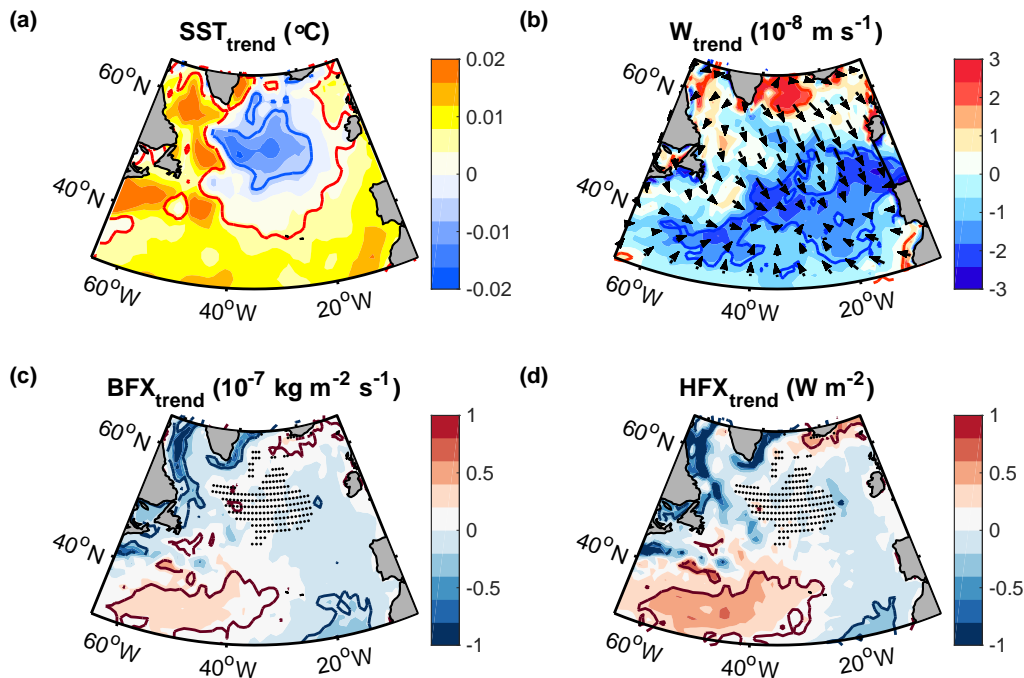
Figure A3. Trends of (a) the SST, (b) the vertical Ekman velocity (positive upward), (c) the buoyancy fluxes (positive downward) and (d) the surface fluxes in winter (January through March). The arrows in (b) indicate the direction of the horizontal Ekman transports and the dots in (c) and (d) mark the region of the mass balance calculation. Contours delineate the regions that are significant at the 95% confidence level.

A3 Comparison with in-situ observations

To demonstrate the density compensation between temperature and salinity anomalies, we use mixed layer profiles from Argo
floats in the subpolar region (Holte et al., 2017). We focus on the extreme winters 2015 and 2016, which were characterised by
particularly large surface fluxes and deep convection (Yashayaev and Loder, 2017; Piron et al., 2017).

In both winters, the temperature and salinity anomalies are well-correlated with each other ($r \approx 0.72$, $p \approx 5 \cdot 10^{-242}$, based
on 1532 profiles). Moreover, the observed salinity anomalies are well-aligned with the estimated salinity anomalies, obtained
by assuming density compensation (Fig. A4). The root mean square error associated with the mass balance estimate amounts
to $\sim$0.09 g kg^{-1}, which is smaller than that of currently available salinity products (Bao et al., 2019; Xie et al., 2019). This
suggests that even under particularly intense surface fluxes, the additional temperature change achieved by the surface fluxes
is still significantly smaller than the temperature anomalies implied by the freshwater anomalies.
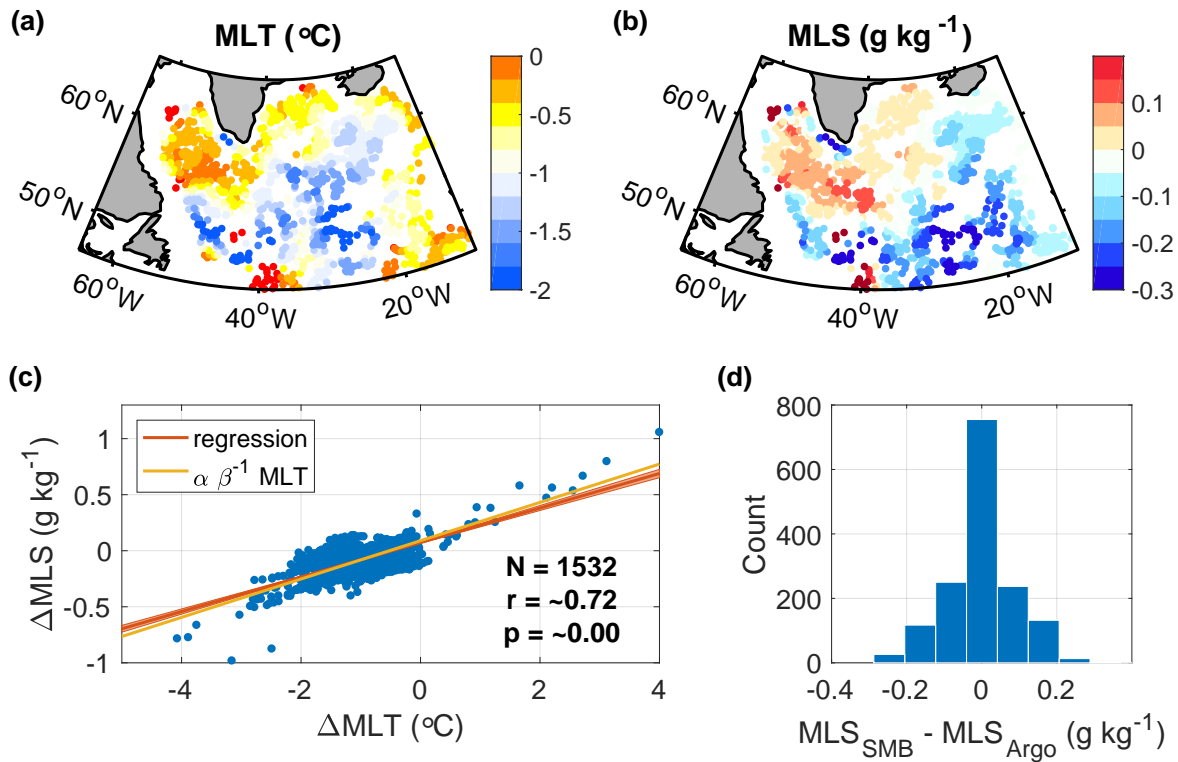
Figure A4. (a,b) Mixed layer temperature (MLT) and salinity (MLS) anomalies in the winters of 2015 and 2016 (January to April), derived
from Argo profiles (Holte et al., 2017). The anomalies are relative to the climatological mean, estimated by averaging all other wintertime
profiles within 2° longitude and 1° latitude. (c) Linear regression of the observed MLS anomalies on the MLT anomalies (red line), and
the MLS estimate obtained by assuming density compensation (yellow line). (d) Differences between the estimated and observed MLS
anomalies. The associated root mean square error is $\sim$0.09 g kg^{-1}.

Appendix B: Simulated atmospheric response to the freshwater-induced SST in winter

To support the role of the SST pattern in driving the observed atmospheric response in winters after freshwater anomalies (Fig. 4b), we define an SST index that captures the time variability of the spatial SST pattern linked to freshwater anomalies. Specifically, we project the SST each winter onto the observed SST pattern after freshwater anomalies (Fig. B1a and b). The projection is obtained from a linear least-square fit of the SST each winter to the observed pattern after freshwater anomalies. We then regress the atmospheric streamfunction at different pressure levels onto this SST index, using 50 ensemble simulations from ECHAM5, performed with prescribed observation-based SSTs.

The SST-forced model simulations support that the SST pattern associated with freshwater anomalies leads to a significant atmospheric circulation anomaly over the North Atlantic, extending deep into the troposphere (Fig. B1c and d). As in the observations, the simulated fields are characterised by a cyclonic circulation anomaly in the subpolar region and an anticyclonic circulation anomaly in the subtropical region. The winds at 250 hPa are still following the underlying SST gradients. Since the simulations were SST-forced, they imply that the obtained atmospheric circulation pattern is driven by the SST, although the SST is itself also the result of atmospheric feedbacks. While a detailed description of the involved diagnostics is beyond the scope of this study, the obtained atmospheric response is consistent with theoretical expectations (Eady, 1949), and the underlying dynamics are well-understood (O'Reilly et al., 2017; Omrani et al., 2019).

We point out that the SST_{FW} pattern (Fig. B1a and b) is specific to the North Atlantic. It was obtained using a projection of the SST each winter onto the SST after freshwater anomalies (Fig. 2a), north of 30 °N. The results are not sensitive to the selected region as long as it includes the enhanced SST front between the subtropical and subpolar gyre. We do not find any significant links of the obtained SST_{FW} pattern to the El Niño Southern Oscillation in the Pacific or to the SST in the South Atlantic.
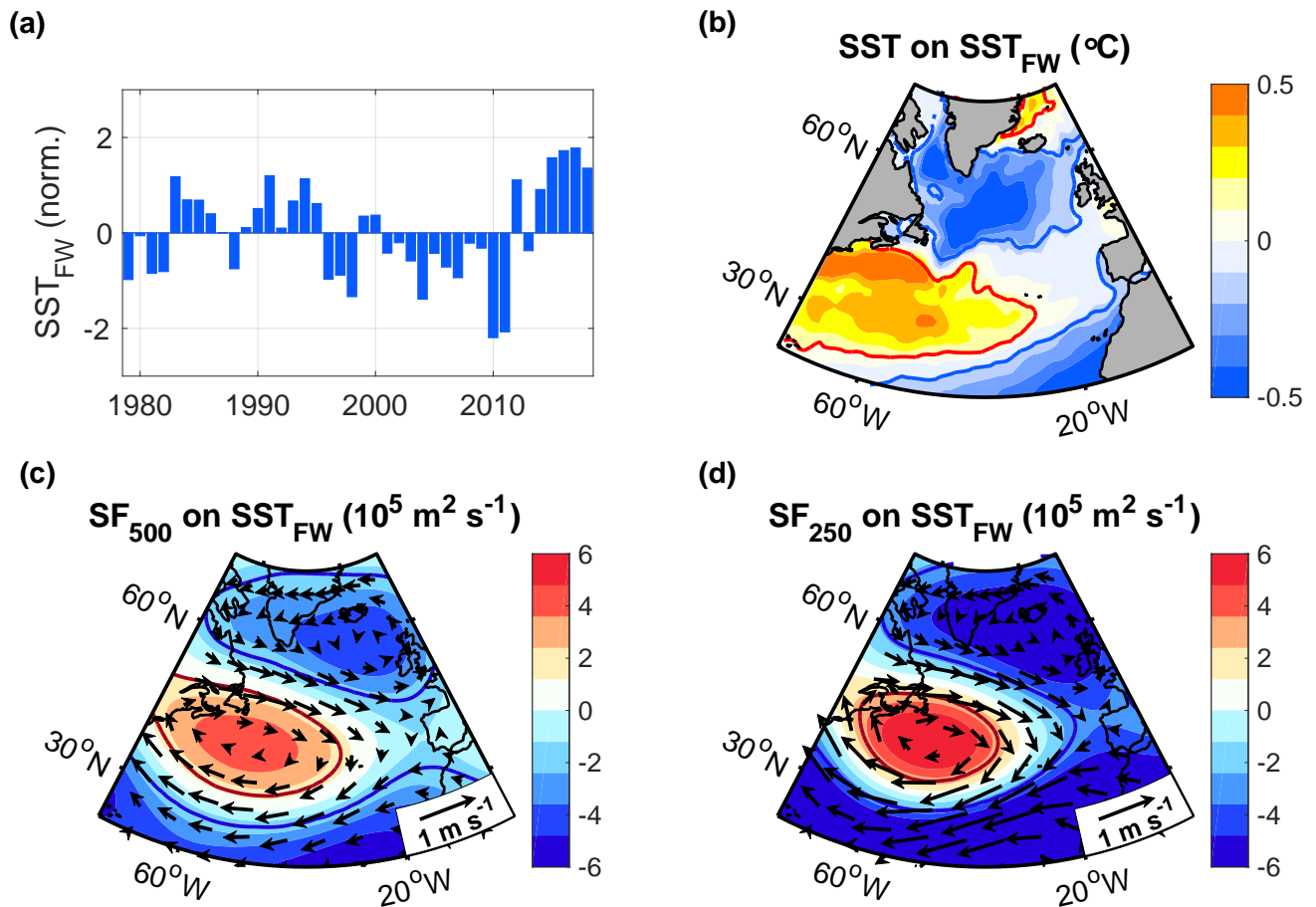
Figure B1. (a) Variability and (b) distribution of the freshwater-induced SST pattern in winter (January through March), obtained by projecting the SST each winter on the North Atlantic SST (north of 30 °N) after freshwater anomalies (Fig. 2a). Thus, SST_{FW} represents the temporal variability of the spatial SST pattern linked to freshwater anomalies. (c,d) Regressions of the simulated stream function and winds in winter at (c) 500 hPa and (d) 250 hPa onto the normalised SST_{FW} pattern shown in (a) and (b). The simulations were acquired from 50 ensemble members from ECHAM5, performed with prescribed observation-based SST over the period 1979–2018. Contours encompass regions that are significant at the 95% confidence level.

Appendix C: Evolution and extent of the summer cold anomaly

Section 4.7 showed that wind driven transports in summers after reduced NAO states are consistent with the associated SST signal and thus likely contribute to it (Fig. 10a). We also examined the surface heat fluxes. While the surface heat fluxes may contribute to some cooling of the central North Atlantic in May and June, they are weakly positive over the cold anomaly region in July, when the cold anomaly is strongest (Fig. C1). A positive surface heat flux anomaly implies that the ocean anomalously cools the lower troposphere rather than the other way round, suggesting that the contribution of the surface heat fluxes to the cold anomaly may be limited.

To assess the role of the atmospheric forcing for the development of the SST signal, we examined the vertical extent and evolution of the ocean signal with in-situ observations from Argo floats from the cold anomaly region (Fig. C2a). Due to the large spatial variability in this region, associated with shifts in the North Atlantic Current and eddies, it is not meaningful to construct time series of absolute temperature and salinity variability. The large spatial variability does not allow to deduce the temporal variability with sufficient accuracy. Therefore, we use vertical density gradients, representing stratification. Vertical gradients are spatially more uniform as they are typically linked to the surface forcing, which equally affects eddies, currents, or other spatially heterogenous regions. Thus, it is possible to construct continuous time series (Fig. C2b).

Next, we regress the obtained time series onto the summer NAO from the preceding year. We find a significant decrease in stratification that peaks near the surface, in the upper 50 m (Fig. C2c). The shallowness of the signal is consistent with wind-induced upwelling. Moreover, the signal is strongest in July and August, when the temperature contrast across the coastline, and the temperature contrast between regions of upwelling and downwelling, is largest. Thus, the timing of the anomaly supports the role air-sea coupling in intensifying the cold anomaly signal (Section 4.7).

Author contributions. M.O. conceived the study, carried out the analyses and was lead writer of the text. P.H. facilitated the implementation of the study; J.S. provided guidance in the model analysis; S.B. helped to revise the paper.

Competing interests. The authors declare that they have no conflict of interest.

Acknowledgements. We thank NOAA/OAR/ESRL and the Hadley Centre for providing the SST data, the Copernicus Marine Service for distributing the altimetry products, the European Centre for Medium-Range Weather Forecasts for developing the reanalysis ERA5 product, and the NOAA Physical Sciences Laboratory for facilitating access to the climate model outputs. We also thank Xavier Fettweis for providing output from the Greenland climate model MAR. The Argo data were collected and made freely available by the international Argo project and the national programs that contribute to it (http://doi.org/10.17882/42182). This study was funded through the grants ACSIS (NE/N018044/1), CLASS (NE/R015953/1) and CANARI (NE/W004984/1) from the UK National Environmental Research Council.
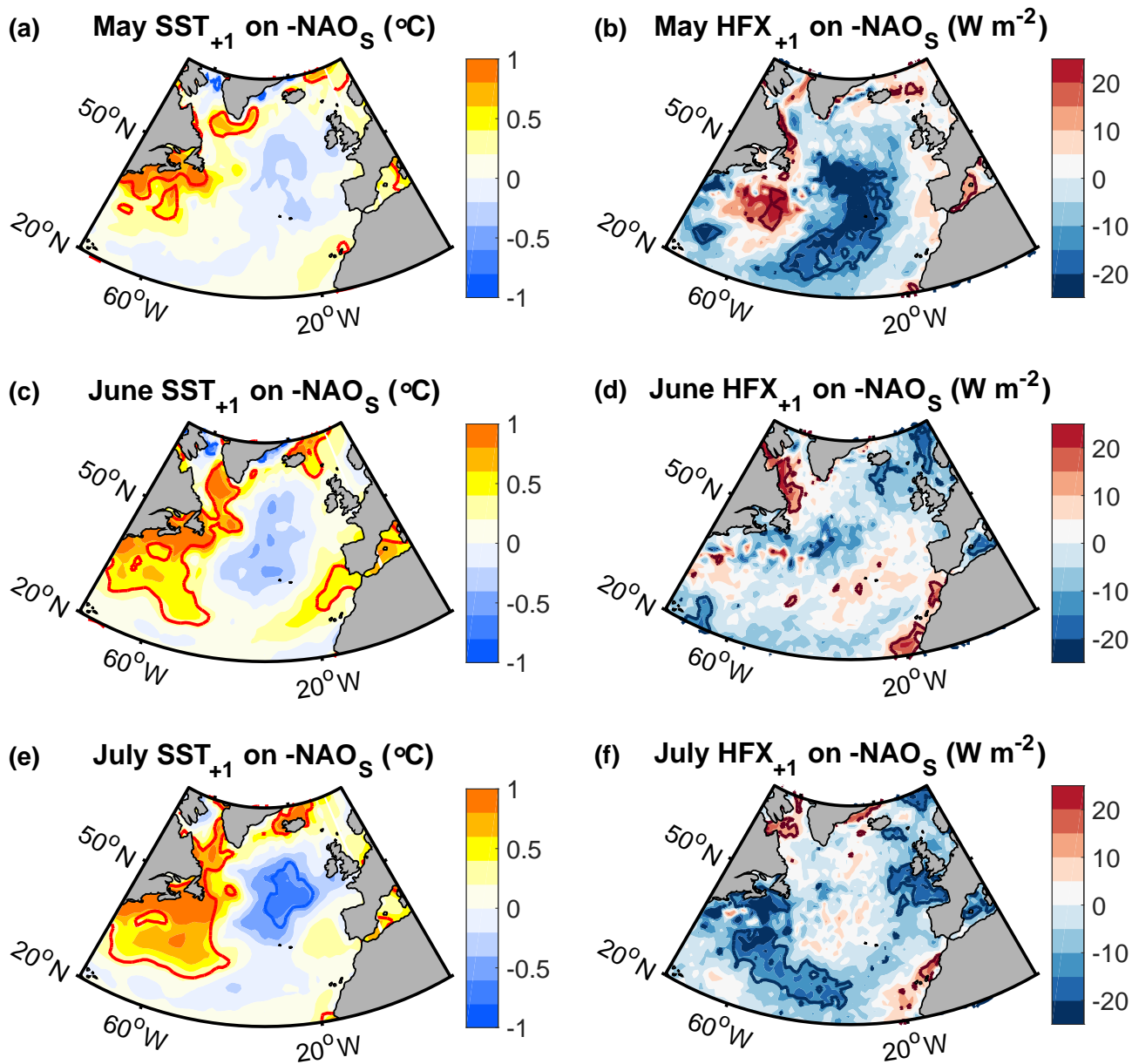
Figure C1. Regression of (a,c,e) the SST and (b,d,f) the surface heat fluxes in (a,b) May, (c,d) June and (e,f) July on $-\mathrm{NAO}_S$ from the preceding year. Thick contours encompass regions that are significant at the 95% level.
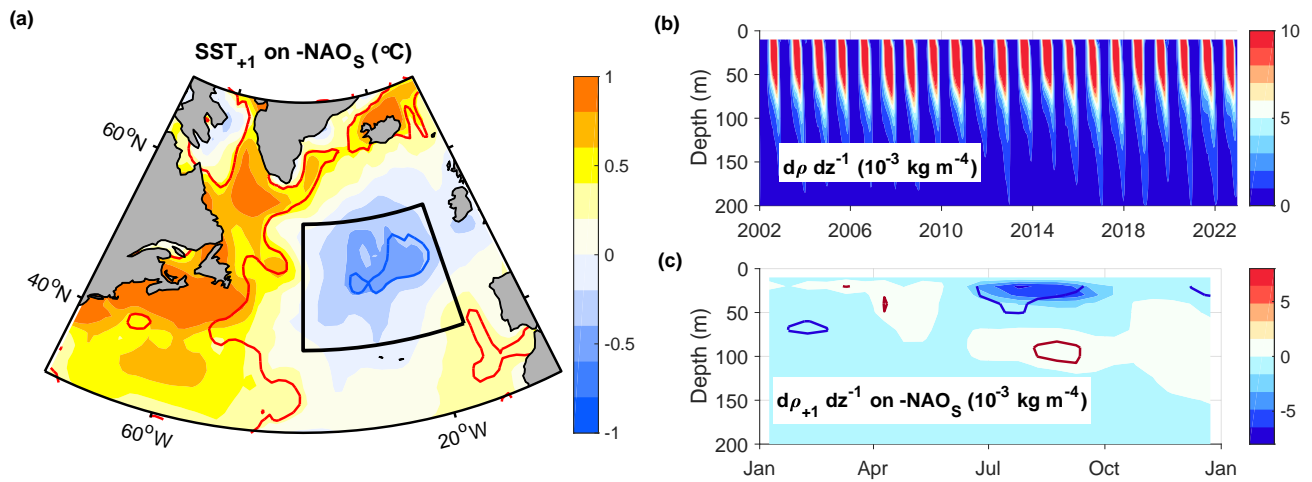
Figure C2. (a) Regression of the SST, averaged from May to August, onto $-\mathrm{NAO}_S$ in July and August from the preceding year. (b) Time series of the vertical density gradient, obtained from Argo floats inside the box shown in (a), averaged within 2-week time windows, and smoothed by applying a 6-week running mean. (c) Regression of the time series in (b) onto $-\mathrm{NAO}_S$ from the preceding year. Thick contours encompass regions that are significant at the 95% confidence level.

References

Arribas, A., Glover, M., Maidens, A., Peterson, K., Gordon, M., MacLachlan, C., Graham, R., Fereday, D., Camp, J., Scaife, A., et al.: The GloSea4 ensemble prediction system for seasonal forecasting, Monthly Weather Review, 139, 1891–1910, 2011.

Bamber, J., Tedstone, A., King, M., Howat, I., Enderlin, E., van den Broeke, M., and Noel, B.: Land ice freshwater budget of the Arctic and North Atlantic Oceans: 1. Data, methods, and results, Journal of Geophysical Research: Oceans, 123, 1827–1837, 2018.

Bao, S., Wang, H., Zhang, R., Yan, H., and Chen, J.: Comparison of satellite-derived sea surface salinity products from SMOS, Aquarius, and SMAP, Journal of Geophysical Research: Oceans, 124, 1932–1944, 2019.

Barnes, E. A.: Revisiting the evidence linking Arctic amplification to extreme weather in midlatitudes, Geophysical research letters, 40, 4734–4739, 2013.

Barnston, A. G. and Livezey, R. E.: Classification, seasonality and persistence of low-frequency atmospheric circulation patterns, Monthly weather review, 115, 1083–1126, 1987.

Blackport, R. and Screen, J. A.: Insignificant effect of Arctic amplification on the amplitude of midlatitude atmospheric waves, Science advances, 6, eaay2880, 2020.

Böning, C. W., Behrens, E., Biastoch, A., Getzlaff, K., and Bamber, J. L.: Emerging impact of Greenland meltwater on deepwater formation in the North Atlantic Ocean, Nature Geoscience, 9, 523–527, 2016.

Briner, J. P., Cuzzone, J. K., Badgeley, J. A., Young, N. E., Steig, E. J., Morlighem, M., Schlegel, N.-J., Hakim, G. J., Schaefer, J. M., Johnson, J. V., et al.: Rate of mass loss from the Greenland Ice Sheet will exceed Holocene values this century, Nature, 586, 70–74, 2020.

Carmack, E. C., Yamamoto-Kawai, M., Haine, T. W., Bacon, S., Bluhm, B. A., Lique, C., Melling, H., Polyakov, I. V., Straneo, F., Timmermans, M.-L., et al.: Freshwater and its role in the Arctic Marine System: Sources, disposition, storage, export, and physical and biogeochemical consequences in the Arctic and global oceans, Journal of Geophysical Research: Biogeosciences, 121, 675–717, 2016.

Cohen, J., Screen, J. A., Furtado, J. C., Barlow, M., Whittleston, D., Coumou, D., Francis, J., Dethloff, K., Entekhabi, D., Overland, J., et al.: Recent Arctic amplification and extreme mid-latitude weather, Nature geoscience, 7, 627–637, 2014.

Cohen, J., Zhang, X., Francis, J., Jung, T., Kwok, R., Overland, J., Ballinger, T., Bhatt, U., Chen, H., Coumou, D., et al.: Divergent consensuses on Arctic amplification influence on midlatitude severe winter weather, Nature Climate Change, pp. 1–10, 2019.

Czaja, A. and Frankignoul, C.: Observed impact of Atlantic SST anomalies on the North Atlantic Oscillation, Journal of Climate, 15, 606–623, 2002.

Davies, H. and Bishop, C.: Eady edge waves and rapid development, Journal of the atmospheric sciences, 51, 1930–1946, 1994.

Dierer, S., Schluenzen, K. H., et al.: Influence parameters for a polar mesocyclone development, METEOROLOGISCHE ZEITSCHRIFT-BERLIN-, 14, 781, 2005.

Dong, B., Sutton, R. T., Woollings, T., and Hodges, K.: Variability of the North Atlantic summer storm track: Mechanisms and impacts on European climate, Environmental Research Letters, 8, 034 037, 2013.

Duchez, A., Frajka-Williams, E., Josey, S. A., Evans, D. G., Grist, J. P., Marsh, R., McCarthy, G. D., Sinha, B., Berry, D. I., and Hirschi, J. J.: Drivers of exceptionally cold North Atlantic Ocean temperatures and their link to the 2015 European heat wave, Environmental Research Letters, 11, 074 004, 2016.

Dukhovskoy, D., Yashayaev, I., Proshutinsky, A., Bamber, J., Bashmachnikov, I., Chassignet, E., Lee, C., and Tedstone, A.: Role of Greenland freshwater anomaly in the recent freshening of the subpolar North Atlantic, Journal of Geophysical Research: Oceans, 124, 3333–3360, 2019.

Dunstone, N., Smith, D., Scaife, A., Hermanson, L., Fereday, D., O'Reilly, C., Stirling, A., Eade, R., Gordon, M., MacLachlan, C., et al.: Skilful seasonal predictions of summer European rainfall, Geophysical Research Letters, 45, 3246–3254, 2018.

700 Eady, E. T.: Long waves and cyclone waves, Tellus, 1, 33–52, 1949.

Fettweis, X., Box, J. E., Agosta, C., Amory, C., Kittel, C., Lang, C., van As, D., Machguth, H., and Gallée, H.: Reconstructions of the 1900–2015 Greenland ice sheet surface mass balance using the regional climate MAR model, The Cryosphere, 11, 1015–1033, 2017.

Francis, J. A. and Vavrus, S. J.: Evidence linking Arctic amplification to extreme weather in mid-latitudes, Geophysical research letters, 39, 2012.

705 Fratantoni, P. S. and McCartney, M. S.: Freshwater export from the Labrador Current to the North Atlantic Current at the Tail of the Grand Banks of Newfoundland, Deep Sea Research Part I: Oceanographic Research Papers, 57, 258–283, 2010.

Gervais, M., Shaman, J., and Kushnir, Y.: Impact of the North Atlantic Warming Hole on Sensible Weather, Journal of Climate, 33, 4255–4271, 2020.

Gill, A. E.: Atmosphere—ocean dynamics, Elsevier, 2016.

710 Häkkinen, S.: Freshening of the Labrador Sea surface waters in the 1990s: Another great salinity anomaly?, Geophysical Research Letters, 29, 85–1, 2002.

Häkkinen, S. and Rhines, P. B.: Shifting surface currents in the northern North Atlantic Ocean, Journal of Geophysical Research: Oceans, 114, 2009.

Häkkinen, S., Rhines, P. B., and Worthen, D. L.: Warm and saline events embedded in the meridional circulation of the northern North Atlantic, Journal of Geophysical Research: Oceans, 116, 2011a.

715 Häkkinen, S., Rhines, P. B., and Worthen, D. L.: Atmospheric blocking and Atlantic multidecadal ocean variability, Science, 334, 655–659, 2011b.

Häkkinen, S., Rhines, P. B., and Worthen, D. L.: Northern North Atlantic sea surface height and ocean heat content variability, Journal of Geophysical Research: Oceans, 118, 3670–3678, 2013.

720 Hanna, E., Jones, J. M., Cappelen, J., Mernild, S. H., Wood, L., Steffen, K., and Huybrechts, P.: The influence of North Atlantic atmospheric and oceanic forcing effects on 1900–2010 Greenland summer climate and ice melt/runoff, International Journal of Climatology, 33, 862–880, 2013.

Hanna, E., Cappelen, J., Fettweis, X., Mernild, S. H., Mote, T. L., Mottram, R., Steffen, K., Ballinger, T. J., and Hall, R. J.: Greenland surface air temperature changes from 1981 to 2019 and implications for ice-sheet melt and mass-balance change, International Journal of 725 Climatology, 41, E1336–E1352, 2021.

Hersbach, H., Bell, B., Berrisford, P., Biavati, G., Horányi, A., Muñoz Sabater, J., Nicolas, J., Peubey, C., Radu, R., Rozum, I., et al.: ERA5 hourly data on single levels from 1979 to present, Copernicus Climate Change Service (C3S) Climate Data Store (CDS), 10, 2018.

Heuzé, C.: North Atlantic deep water formation and AMOC in CMIP5 models, Ocean Science, 13, 609, 2017.

Holliday, N. P., Bersch, M., Berx, B., Chafik, L., Cunningham, S., Florindo-López, C., Hátún, H., Johns, W., Josey, S. A., Larsen, K. M. H., 730 et al.: Ocean circulation causes the largest freshening event for 120 years in eastern subpolar North Atlantic, Nature Communications, 11, 1–15, 2020.

Holte, J., Talley, L. D., Gilson, J., and Roemmich, D.: An Argo mixed layer climatology and database, Geophysical Research Letters, 44, 5618–5626, 2017.

Hurrell, J. W., Hack, J. J., Shea, D., Caron, J. M., and Rosinski, J.: A new sea surface temperature and sea ice boundary dataset for the 735 Community Atmosphere Model, Journal of Climate, 21, 5145–5153, 2008.

Khan, S. A., Aschwanden, A., Bjørk, A. A., Wahr, J., Kjeldsen, K. K., and Kjaer, K. H.: Greenland ice sheet mass balance: a review, Reports on progress in physics, 78, 046 801, 2015.

Kostov, Y., Johnson, H. L., Marshall, D. P., Heimbach, P., Forget, G., Holliday, N. P., Lozier, M. S., Li, F., Pillar, H. R., and Smith, T.: Distinct sources of interannual subtropical and subpolar Atlantic overturning variability, Nature Geoscience, 14, 491–495, 2021.

Koul, V., Tesdal, J.-E., Bersch, M., Hátún, H., Brune, S., Borchert, L., Haak, H., Schrum, C., and Baehr, J.: Unraveling the choice of the north Atlantic subpolar gyre index, Scientific reports, 10, 1–12, 2020.

Kumar, A., Yadav, J., and Mohan, R.: Global warming leading to alarming recession of the Arctic sea-ice cover: Insights from remote sensing observations and model reanalysis, Heliyon, 6, e04 355, 2020.

Le Traon, P., Nadal, F., and Ducet, N.: An improved mapping method of multisatellite altimeter data, Journal of atmospheric and oceanic technology, 15, 522–534, 1998.

Lindzen, R. and Farrell, B.: A simple approximate result for the maximum growth rate of baroclinic instabilities, Journal of the atmospheric sciences, 37, 1648–1654, 1980.

Liu, W., Xie, S.-P., Liu, Z., and Zhu, J.: Overlooked possibility of a collapsed Atlantic Meridional Overturning Circulation in warming climate, Science Advances, 3, e1601 666, 2017.

Marshall, J., Johnson, H., and Goodman, J.: A study of the interaction of the North Atlantic Oscillation with ocean circulation, Journal of Climate, 14, 1399–1421, 2001.

Marzocchi, A., Hirschi, J. J.-M., Holliday, N. P., Cunningham, S. A., Blaker, A. T., and Coward, A. C.: The North Atlantic subpolar circulation in an eddy-resolving global ocean model, Journal of Marine Systems, 142, 126–143, 2015.

Mecking, J., Drijfhout, S., Jackson, L., and Andrews, M.: The effect of model bias on Atlantic freshwater transport and implications for AMOC bi-stability, Tellus A: Dynamic Meteorology and Oceanography, 69, 1299 910, 2017.

Mecking, J., Drijfhout, S., Hirschi, J. J., and Blaker, A.: Ocean and atmosphere influence on the 2015 European heatwave, Environmental Research Letters, 14, 114 035, 2019.

Menary, M. B., Hodson, D. L., Robson, J. I., Sutton, R. T., Wood, R. A., and Hunt, J. A.: Exploring the impact of CMIP5 model biases on the simulation of North Atlantic decadal variability, Geophysical Research Letters, 42, 5926–5934, 2015.

Müller, V., Kieke, D., Myers, P. G., Pennelly, C., Steinfeldt, R., and Stendardo, I.: Heat and freshwater transport by mesoscale eddies in the southern subpolar North Atlantic, Journal of Geophysical Research: Oceans, 124, 5565–5585, 2019.

Munk, W. H.: On the wind-driven ocean circulation, Journal of Atmospheric Sciences, 7, 80–93, 1950.

Murray, D., Hoell, A., Hoerling, M., Perlwitz, J., Quan, X.-W., Allured, D., Zhang, T., Eischeid, J., Smith, C. A., Barsugli, J., et al.: Facility for Weather and Climate Assessments (FACTS): A Community Resource for Assessing Weather and Climate Variability, Bulletin of the American Meteorological Society, 101, E1214–E1224, 2020.

Neale, R. B., Chen, C.-C., Gettelman, A., Lauritzen, P. H., Park, S., Williamson, D. L., Conley, A. J., Garcia, R., Kinnison, D., Lamarque, J.-F., et al.: Description of the NCAR community atmosphere model (CAM 5.0), NCAR Tech. Note NCAR/TN-486+ STR, 1, 1–12, 2012.

Notz, D. and Stroeve, J.: The trajectory towards a seasonally ice-free Arctic ocean, Current climate change reports, 4, 407–416, 2018.

Oltmanns, M., Karstensen, J., Moore, G., and Josey, S. A.: Rapid cooling and increased storminess triggered by freshwater in the North Atlantic, Geophysical Research Letters, p. e2020GL087207, 2020.

Omrani, N.-E., Ogawa, F., Nakamura, H., Keenlyside, N., Lubis, S. W., and Matthes, K.: Key Role of the Ocean Western Boundary currents in shaping the Northern Hemisphere climate, Scientific reports, 9, 1–12, 2019.

O'Reilly, C. H., Minobe, S., Kuwano-Yoshida, A., and Woollings, T.: The Gulf Stream influence on wintertime North Atlantic jet variability, Quarterly Journal of the Royal Meteorological Society, 143, 173–183, 2017.

775 Osborne, J. M., Collins, M., Screen, J. A., Thomson, S. I., and Dunstone, N.: The North Atlantic as a driver of summer atmospheric circulation, Journal of Climate, 33, 7335–7351, 2020.

Overland, J., Francis, J. A., Hall, R., Hanna, E., Kim, S.-J., and Vihma, T.: The melting Arctic and midlatitude weather patterns: Are they connected?, Journal of Climate, 28, 7917–7932, 2015.

Piron, A., Thierry, V., Mercier, H., and Caniaux, G.: Gyre-scale deep convection in the subpolar North Atlantic Ocean during winter 2014–
780 2015, Geophysical Research Letters, 44, 1439–1447, 2017.

Proshutinsky, A., Dukhovskoy, D., Timmermans, M.-L., Krishfield, R., and Bamber, J. L.: Arctic circulation regimes, Philosophical Transactions of the Royal Society A: Mathematical, Physical and Engineering Sciences, 373, 20140 160, 2015.

Rayner, N., Parker, D. E., Horton, E., Folland, C. K., Alexander, L. V., Rowell, D., Kent, E., and Kaplan, A.: Global analyses of sea surface temperature, sea ice, and night marine air temperature since the late nineteenth century, Journal of Geophysical Research: Atmospheres,
785 108, 2003.

Reynolds, R. W., Rayner, N. A., Smith, T. M., Stokes, D. C., and Wang, W.: An improved in situ and satellite SST analysis for climate, Journal of climate, 15, 1609–1625, 2002.

Roeckner, E., Bäuml, G., Bonaventura, L., Brokopf, R., Esch, M., Giorgetta, M., Hagemann, S., Kirchner, I., Kornblueh, L., Manzini, E., et al.: The atmospheric general circulation model ECHAM 5. PART I: Model description, Accessed March 2020., 2003.

790 Schmidt, S. and Send, U.: Origin and composition of seasonal Labrador Sea freshwater, Journal of Physical Oceanography, 37, 1445–1454, 2007.

Screen, J. A. and Simmonds, I.: Exploring links between Arctic amplification and mid-latitude weather, Geophysical Research Letters, 40, 959–964, 2013.

Sgubin, G., Swingedouw, D., Drijfhout, S., Mary, Y., and Bennabi, A.: Abrupt cooling over the North Atlantic in modern climate models,
795 Nature Communications, 8, 14 375, 2017.

Spall, M. A. and Pickart, R. S.: Wind-driven recirculations and exchange in the Labrador and Irminger Seas, Journal of Physical Oceanography, 33, 1829–1845, 2003.

Stommel, H.: The westward intensification of wind-driven ocean currents, Eos, Transactions American Geophysical Union, 29, 202–206, 1948.

800 Tang, Q., Zhang, X., and Francis, J. A.: Extreme summer weather in northern mid-latitudes linked to a vanishing cryosphere, Nature Climate Change, 4, 45–50, 2014.

Tesdal, J.-E., Abernathey, R. P., Goes, J. I., Gordon, A. L., and Haine, T. W.: Salinity trends within the upper layers of the subpolar North Atlantic, Journal of Climate, 31, 2675–2698, 2018.

Timlin, M. S., Alexander, M. A., and Deser, C.: On the reemergence of North Atlantic SST anomalies, Journal of climate, 15, 2707–2712,
805 2002.

Vallis, G. K.: Atmospheric and oceanic fluid dynamics, Cambridge University Press, 2017.

Woollings, T., Hannachi, A., and Hoskins, B.: Variability of the North Atlantic eddy-driven jet stream, Quarterly Journal of the Royal Meteorological Society, 136, 856–868, 2010.

Wu, Y., Park, T., Park, W., and Latif, M.: North Atlantic climate model bias influence on multiyear predictability, Earth and Planetary Science
810 Letters, 481, 171–176, 2018.

Xie, J., Raj, R. P., Bertino, L., Samuelsen, A., and Wakamatsu, T.: Evaluation of Arctic Ocean surface salinities from the Soil Moisture and Ocean Salinity (SMOS) mission against a regional reanalysis and in situ data, Ocean Science, 15, 1191–1206, 2019.

Yashayaev, I. and Loder, J. W.: Further intensification of deep convection in the Labrador Sea in 2016, Geophysical Research Letters, 44, 1429–1438, 2017.

815 Zhao, J. and Johns, W.: Wind-forced interannual variability of the Atlantic Meridional Overturning Circulation at 26.5 N, Journal of Geophysical Research: Oceans, 119, 2403–2419, 2014.